

Supplementary Information

Non-Plasmonic Ni Nanoparticles Catalyzed Visible Light Selective Hydrogenolysis of Aryl Ethers in Lignin under Mild Conditions

Peifeng Li,^{#,a} Yixuan Ouyang,^{#,a} Gang Xiao,^{,a} Yilin Zhao,^a Sarina Sarina,^b Jan Baeyens,^{c,d} Haijia Su,^{*,a} and Huai-Yong Zhu^b*

^aState Key Laboratory of Chemical Resource Engineering, Beijing Key Laboratory of Bioprocess, College of Life Science and Technology, Beijing University of Chemical Technology, Beijing 100029, PR China

^bSchool of Chemistry, Physics and Mechanical Engineering, Queensland University of Technology, Brisbane 4001, Australia

^cBeijing Advanced Innovation Centre for Smart Matter and Engineering, Beijing University of Chemical Technology, Beijing 100029, PR China

^dFaculty of Engineering Technology, KU Leuven, 2860 Sint-Katelijne-Waver, Belgium

[#]These authors contributed equally.

^{*}Corresponding to: sewicxiao@hotmail.com, xiaogang@mail.buct.edu.cn (G. Xiao) and suhj@mail.buct.edu.cn (H. Su)

Table of Contents

1. Background Information and Literature Summary	3
1.1. A brief introduction to lignin and its valorization	3
1.2. A literature summary on hydrogenolysis of aryl ethers in lignin	3
1.3. A literature summary on photocatalytic cleavage of aryl ethers in lignin	5
1.4. A brief introduction to light-driven chemical transformations on metal nanoparticles	6
2. Experimental Procedures	9
3. Results and Discussion	13
3.1. Effect of hydrazine hydrate on the hydrogenolysis of BPE catalyzed by Ni/ZrO ₂	13
3.2. Photocatalytic hydrogenolysis of BPE by various catalysts	16
3.3. Photocatalytic hydrogenolysis of BPE in various solvents	17
3.4. Quantification of the identified aromatic monomers from the photocatalytic depolymerization of dealkaline lignin	18
3.5. Characterization of Ni/ZrO ₂ catalysts	20
3.6. Initial rates or TOFs of photocatalytic hydrogenolysis of BPE or PPE under different light conditions and reaction temperatures	22
3.7. Radical scavenger study	24
3.8. Kinetics study for the photocatalytic cleavage of PP-one	25
3.9. Recycling of the Ni/ZrO ₂ catalyst	26
4. References	27

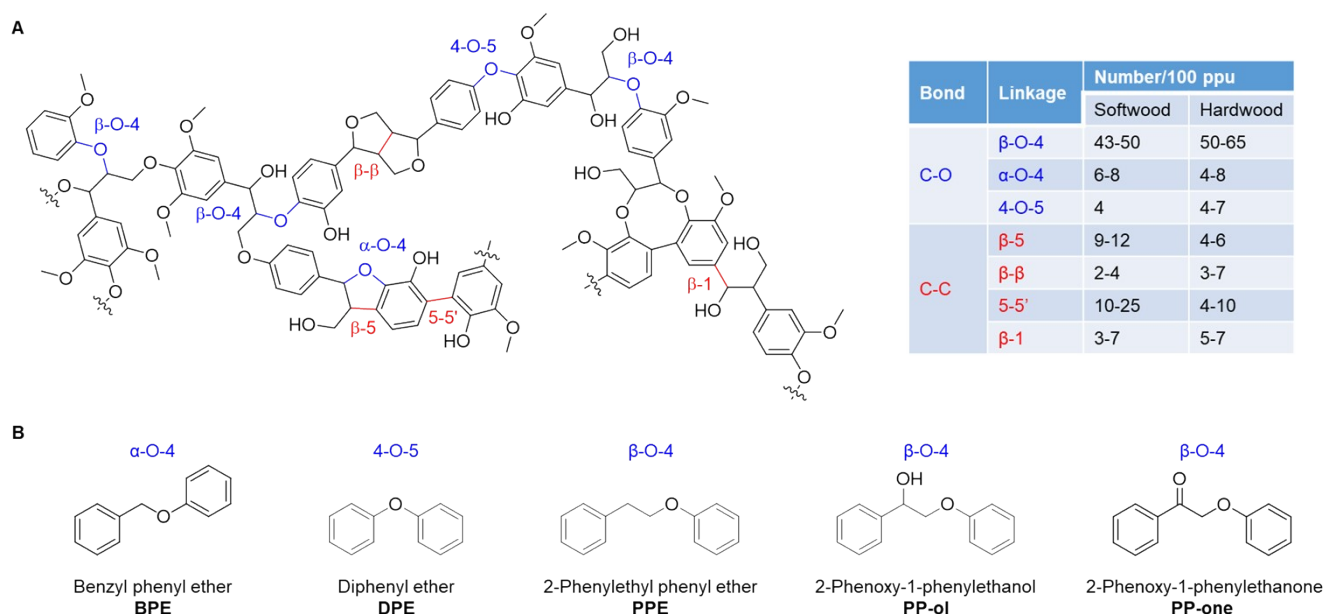
1. Background Information and Literature Summary

1.1. A brief introduction to lignin and its valorization

The world-wide energy crisis and related environmental concerns have motivated extensive research interest on biomass conversion.^[1] The carbon-neutral and inedible lignocellulose is the most abundant form of biomass, with a global production of about 170 billion metric tons per year.^[2,3] It has been widely accepted to be a promising alternative to fossil resources for the production of bio-derived fuels, chemicals, and materials through biorefinery.^[4] In order to make an industrial scale biorefinery process cost-competitive, it is essential to valorize all the three components of lignocellulose: cellulose, hemicellulose, and lignin.^[5,6] However, current biorefinery process focuses on the transformation of the two carbohydrate components, cellulose and hemicellulose, leaving lignin far underutilized and environmental hazardous.^[6]

Lignin is a complex three-dimensional macromolecule that holds the raw lignocellulosic matrix together and adds strength and rigidity to the system.^[1,4] It is an amorphous and water-insoluble aromatic polymer composed of three primary units: sinapyl, coniferyl, and *p*-coumaryl alcohols, which are also known as syringyl (S), guaiacyl (G), and *p*-hydroxy-phenyl (H) units, respectively.^[4] Lignin monolignols are predominantly cross-linked by C-O bonds, including β -O-4, α -O-4, and 4-O-5 ether linkages, and additionally by C-C bonds.^[7] Scheme S1a presents the typical lignin structure and linkages with the amount of each linkage.^[6,8] In Scheme S1a, ppu means a phenylpropane unit which is the typical aromatic unit in lignin because all the three monolignols contain a phenyl group and a propyl side-chain. Due to the highly-functionalized and aromatic nature, lignin presents the potential for the direct preparation of aromatic platform chemicals and more valuable specialty and fine chemicals.^[9] It is the only naturally occurred renewable aromatic source in large-volume and has been recognized as the promising candidate to produce value-added aromatics.^[10] Selective cleavage of these linkages, especially the dominate C-O ether linkages, through various catalysis procedures, is essential to achieve the valorization of lignin and production of aromatic chemicals.^[11] Although extensive efforts have been paid on this research topic recently, it remains a great challenge to obtain satisfactory yield of desired aromatic products under mild conditions.^[2,6,8] Therefore, it is necessary to intensively study the selective bond cleavage of each linkage to generate new knowledge on bond properties and their cleavage mechanisms.^[6] Lignin dimer models which mimic lignin linkages are recognized as good choices for fundamentally studying the selective bond cleavage. Scheme S1b presents five commonly used dimer model compounds mimicking the three C-O ether linkages. 2-Phenylethyl phenyl ether (PPE), benzyl phenyl ether (BPE), and diphenyl ether (DPE) are the simplest dimer models without substitutions for the β -O-4, α -O-4, and 4-O-5 linkages, respectively. They are widely adopted to fundamentally study the selective cleavage of C-O ether linkages in lignin, because more complex substitutions hardly influence the principal chemistry.^[12-15] The other two β -O-4 model compounds, 2-phenoxy-1-phenylethanol (PP-ol) and 2-phenoxy-1-phenylethanone (PP-one), which bears C_{α} alcohol and C_{α} ketone, respectively, are also commonly used. This is because the two substitutes at C_{α} position have been proven to affect the cleavage of β -O-4 linkage significantly in several catalysis systems.^[16-18]

For further information, please refer to some of the recently published excellent review articles.^[1,2,4,5,6,8,9,11]



Scheme S1. Lignin and dimer model compounds

(A) A representative lignin structure displaying typical C-O (in blue) and C-C (in red) linkages with the amount of each linkage in softwood and hardwood lignin.^[6,8] (B) Typical dimer model compounds which mimic three type lignin C-O ether linkages.^[12-18]

1.2. A literature summary on hydrogenolysis of aryl ethers in lignin

Selective hydrogenolysis of aryl ether ($C_{\text{aryl}}\text{-O}$) bonds in lignin is one of the most promising methods to produce value-added aromatic chemicals from lignin.^[19] Table S1 presents the recently reported catalysts and their performance in catalyzing the hydrogenolysis of aryl ether bonds in lignin.^[13-15,20-34] Among various precious (Ru, Rh, Pd) and non-precious (Ni, Fe) metal catalysts, Ni is the most promising one. Although its activity is moderate, the low-cost Ni generally shows higher selectivity towards hydrogenolysis than

precious metals, which will facilitate the production of aromatics rather than the undesired saturated products.^[7] Since the seminal work by Sergeev and Hartwig in 2011^[26], various Ni catalysts have been developed. However, it remains a great challenge to achieve the selective hydrogenolysis of aryl ether bonds without de-aromatization under mild conditions. In the present study, we cleaved the three aryl ether bonds at very mild conditions with excellent conversion and good to excellent selectivity using a robust Ni/ZrO₂ catalyst and visible light (Table S1, Entry 51-56). For the α -O-4 model, BPE and two β -O-4 models, PP-ol and PP-one, both excellent conversion and high selectivity can be obtained at room temperature (Table S1, Entry 51,54-56).

Table S1. Representative results for hydrogenolysis of lignin model compounds using various catalysts.

Entry	Catalysts	Reaction conditions	Reactant	Conversion (%)	TOF (h ⁻¹)	Yield (%) ^a	Ref.
Catalysts containing precious metals							
1	Ru-W/AC	<i>n</i> -hexane, H ₂ 0.7 MPa, 260 °C, 10 h	BPE	99.7	N.A.	78.2	[20]
2	Rh NPs	10 mol% NPs, H ₂ O, 10 bar H ₂ , 60 °C, 1 h	BPE	100	10 ^b	0	[21]
3	NiOx/Rh NPs			66	6.6 ^b	65	
4	Pd-Ni@ZrO ₂	NaBH ₄ , ethanol, 80 °C, 6 h	PP-ol	100	0.75 ^b	96	[22]
5			BPE	100	2.03 ^b	>99	
6	Pd/Ni	isopropanol, H ₂ 10 bar, 210 °C, 90 min	PPE	75	1.42 ^b	70	[15]
7			DPE	73	1.61 ^b	53	
8		isopropanol, 120 °C, 10 h	BPE	>99	2.02 ^b	52	
9	Ru/C	isopropanol, NaOtBu, 180 °C, 24 h	PPE	>99	0.84 ^b	56	[23]
10		isopropanol, 120 °C, 10 h	DPE	>99	2.02 ^b	33.2	
11		isopropanol, 150 °C, 10 h	PP-ol	66.7	1.35 ^b	26	
12	Pd/Fe ₃ O ₄	isopropanol, N ₂ 10 bar, 240 °C, 6 h	BPE	100	13.2 ^c	100	[24]
13		Ru ₁₅ Ni ₈₅ , H ₂ O, H ₂ 1 atm, 95 °C, 16 h	BPE			74	
14			PPE			55	
15	Ru-Ni (CTAB) NPs	Ru ₆₀ Ni ₄₀ , H ₂ O, H ₂ 1 atm, 95 °C, 16 h	DPE	>99	1.25 ^b	28	
16		Ru ₁₅ Ni ₈₅ , H ₂ O, H ₂ 1 atm, 95 °C, 16 h	PP-ol			53	
17			PP-one			57	[14]
18		Rh ₁₅ Ni ₈₅ , H ₂ O, H ₂ 1 atm, 95 °C, 16 h	BPE	100	1.25 ^b	90	
19			PPE	97	1.21 ^b	80	
20	Rh-Ni (CTAB) NPs	Rh ₆₀ Ni ₄₀ , H ₂ O, H ₂ 1 atm, 95 °C, 16 h	DPE	>99	1.25 ^b	20.5	
21		Rh ₁₅ Ni ₈₅ , H ₂ O, H ₂ 1 atm, 95 °C, 16 h	PP-ol	>99	1.25 ^b	80	
22			PP-one	100	1.25 ^b	90	
23		methanol, H ₂ 0.5 MPa, 120 °C, 2 h	BPE	100	3.01 ^b	95	
24	Ni-Ru/AC	methanol, H ₂ 3 MPa, 250 °C, 3 h	PPE	86.2	0.40 ^b	36.4	[25]
25		methanol, H ₂ 4 MPa, 250 °C, 3 h	DPE	86.4	0.47 ^b	33	
Catalysts based on non-precious metals							
26	Ni carbene complex	5-20% Ni(COD) ₂ , 10-40% SIPr-HCl, NaOtBu, <i>m</i> -xylene, 120 °C, 16 h, H ₂ (1 bar at r.t.)	DPE	100	0.31	99	[26]
27	Ni/C	0.5 mol% Ni, NaOtBu, <i>m</i> -xylene, 180 °C, 24 h, H ₂ (1 bar at 22 °C)	DPE	>99	8.33 ^d	99	[27]
28	Heterogeneous "Fe"	20 mol% Fe, LiAlH ₄ , toluene, 140 °C, 24 h	DPE	N.A.	N.A.	98.5	[28]
29			PP-ol	N.A.	N.A.	59	
30	TiN-Ni	ethanol, 12 bar H ₂ , 125 °C, 0.5 mL/min	BPE	>99	0.33 ^d	99	[29]

31			PPE	>99	0.20 ^d	54	
32		ethanol, 12 bar H ₂ , 150 °C, 0.3 mL/min	DPE	99	0.10 ^d	46	
33		H ₂ O, tetra- <i>n</i> -butylammonium bromide (TBAB), KOtBu, 6 bar H ₂ , 90 °C, 20 h	BPE	99	2.1 ^d	98	
34	Ni@SiC		PPE	99	2.1 ^d	95	[30]
35		H ₂ O, tetra- <i>n</i> -butylammonium bromide (TBAB), KOtBu, 6 bar H ₂ , 120 °C, 20 h	DPE	96	0.7 ^d	93	
36			BPE	76	N.A.	71	
37	Ni@IRMOF-74(II)	<i>p</i> -xylene, 10 bar H ₂ , 120 °C, 16 h	PPE	82	N.A.	79	[13]
38			DPE	34	N.A.	29	
39			BPE	100	0.86 ^d	39	
40	NiAlOx	isopropanol, La(OTf) ₃ , 20 bar H ₂ , 120 °C, 2 h	PPE	100	0.86 ^d	38	[31]
41		isopropanol, La(OTf) ₃ , 20 bar H ₂ , 130 °C, 2 h	DPE	N.A.	N.A.	41.5	
42		1:1 water-THF, 2 MPa H ₂ , 240 °C, 12 h	BPE	99	N.A.	95	
43	Fe-L1/C-800	1:1 water-THF, 2 MPa H ₂ , 290 °C, 6 h	PPE	N.A.	N.A.	3	[32]
44			PP-ol	N.A.	N.A.	43	
45		1:1 water-THF, 2 MPa H ₂ , 240 °C, 12 h	PP-one	>99	N.A.	97	
46			BPE	100	16.7 ^d	54	
47	Ti ^{III} ₂ Ti ^{IV} ₆ -NiH	heptane, 1 bar H ₂ , 140 °C, 6 h	PPE	96	16.0 ^d	55	[33]
48		heptane, 1 bar H ₂ , 160 °C, 6 h	DPE	97	16.2 ^d	40	
49		isopropanol, N ₂ 10 bar, 100 °C, 48 h	BPE	100	0.10 ^d	94	[34]
50	Ni/Al ₂ O ₃	isopropanol, N ₂ 10 bar, 150 °C, 12 h	DPE	100	0.40 ^d	37	
51		2-butanol, N ₂ H ₄ ·H ₂ O, r.t., 13 h, LED 0.5 W·cm ⁻²	BPE	99	0.13 ^d	96	
52		2-butanol, N ₂ H ₄ ·H ₂ O, 80 °C, 13 h, LED 0.5 W·cm ⁻²	PPE	95	0.12 ^d	90	
53		isopropanol, N ₂ H ₄ ·H ₂ O, 100 °C, 12 h, LED 0.5 W·cm ⁻²	DPE	95	0.13 ^d	82	
54	Ni/ZrO ₂	2-butanol, N ₂ H ₄ ·H ₂ O, r.t., 15 h, LED 0.5 W·cm ⁻²		96	0.11 ^d	96	This study
55		2-butanol, N ₂ H ₄ ·H ₂ O, r.t., 40 h, sunlight	PP-ol	95	0.04 ^d	95	
56		2-butanol, N ₂ H ₄ ·H ₂ O, r.t., 15 h, LED 0.5 W·cm ⁻²	PP-one	95	0.11 ^d	95	

^aHere presents the carbon yield of aromatic monomers.

^bTOF is calculated based on the total amount of metal.

^cTOF is calculated based on the total amount of Pd.

^dTOF is calculated based on the total amount of Ni.

1.3. A literature summary on photocatalytic cleavage of aryl ethers in lignin

Photocatalytic cleavage of aryl ether (C_{aryl}-O) bonds in lignin is of high potential to achieve solar-to-chemical conversion and lignin valorization simultaneously.^[35] Table S2 presents the performance of recently reported typical photocatalytic procedures for the cleavage of PP-ol.^[17,18,36-38] These photocatalytic procedures, which contain oxidation-hydrogenolysis tandem method, self-hydrogen transfer hydrogenolysis method, and electron-hole coupled photoredox method, are only validate for cleaving β-O-4 bond with the presence of C_α alcohol using ZnIn₂S₄ or CdS based semiconductors (Table S2, Entry 1-6). In the present study, we employed more robust Ni nanoparticles supported on ZrO₂ as photocatalysts and developed a direct hydrogenolysis method by light-driven catalysis (Table S2, Entry 7,8). This method was effective in the selective cleavage of all the three types of aryl C-O bonds (See Table S1, Entry 51-56). When natural conditions (room temperature and sunlight) were used, PP-ol was also effectively cleaved with 95% yield of aromatic monomers (Table S2, Entry 8).

Table S2. Performance of typical photocatalytic procedures for the cleavage of PP-ol.

Entry	Reaction procedure	Catalysts	Reaction conditions	Conversion (%)	TOF (h ⁻¹)	Carbon yield (%)					Ref.
						2	3	4	5	6	

1	A photocatalytic oxidation-hydrogenolysis tandem method in one pot via a dual light wavelength switching strategy	Pd/ZnIn ₂ S ₄ (455 nm), TiO ₂ (365 nm)	ethanol, NaOAc, O ₂ , 5.6 W LED (455 nm for 28 h, then 365 nm for 5 h)	94	N.A.	-	40	43	-	-	[36]
2			ethanol, NaOAc, O ₂ , a mixed light source of 2.8 W 455 and 365 nm LED, 28 h	97	N.A.	-	42	48	-	-	
3	A photocatalytic self-hydrogen transfer hydrogenolysis method	ZnIn ₂ S ₄	CH ₃ CN, 9.6 W LEDs (455 nm), 42 °C, 4 h	>99	2.12 ^a	6	39	47	-	-	[37]
4		Ni/CdS	CH ₃ CN/0.1 M KOH (v/v = 2/8), 8 W blue LED (440-460 nm), 3 h	>99	0.98 ^b	-	43	57	-	-	[38]
5	An electron-hole coupled photoredox mechanism based on a C _α radical intermediate	CdS QDs	CH ₃ CN, N ₂ , 300 W Xe lamp (λ ≥ 420 nm), 3 h	99	0.48	-	40	52	-	-	[17]
6		Ag ₂ S@CdS	CH ₃ CN, 1 atm Ar, 6 W 450 nm LED, 30 °C, 3 h	99	2.30 ^c	4	41	52	-	-	[18]
7	A photocatalytic hydrogenolysis procedure	Ni/ZrO ₂	2-butanol, N ₂ H ₄ ·H ₂ O, r.t., 15 h, LED (400-740 nm) 0.5 W·cm ⁻²	96	0.11 ^b	-	46	-	43	7	This study
8			2-butanol, N ₂ H ₄ ·H ₂ O, r.t., 40 h, sunlight	95	0.04 ^b	-	46	-	44	5	

^aTOF is calculated based on the total amount of Zn.

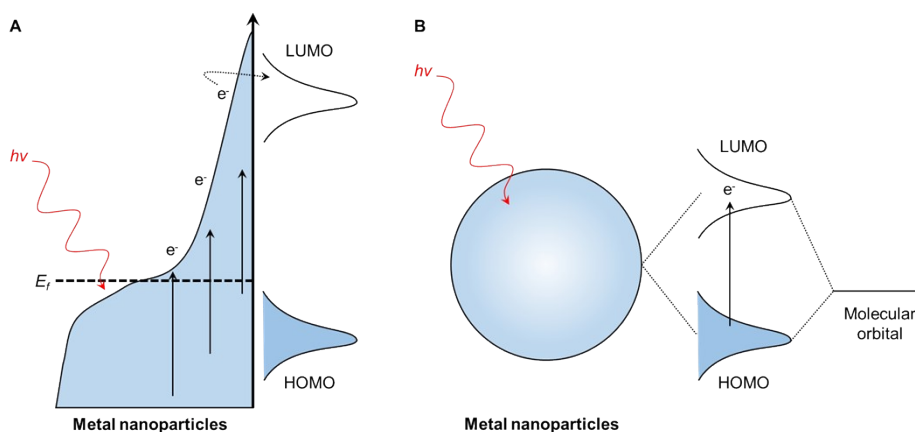
^bTOF is calculated based on the total amount of Ni.

^cTOF is calculated based on the total amount of CdS.

1.4. A brief introduction to light-driven chemical transformations on metal nanoparticles

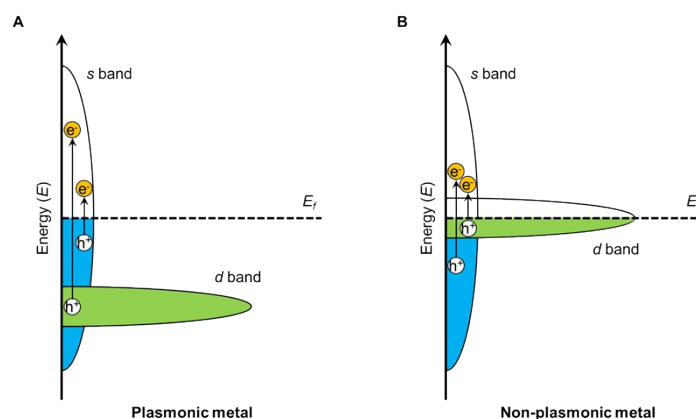
Metal nanoparticles have been widely used as heterogeneous catalysts for a number of industrially important reactions such as partial oxidation, hydrogenation, reforming, and coupling reactions.^[39-41] High temperatures are usually required to overcome the activation energy barrier. Introducing light to drive these reactions on the surface of metal nanoparticles at mild conditions have caused a surge of interest recently.^[42,43] Light can induce the excitation of energetic charge carriers into the adsorbed reactants, which serves as an alternative mechanism for activating chemical bonds on metal surface.^[39,42] Based on this mechanism, the reaction process on metal surface can be tuned by specifically targeting electronic excitations which preferentially activate the desired reaction pathways.^[39,44-46] This unique feature of light-driven chemical transformations on metal nanoparticles is very useful to avoid the unselective formation of by-products and wastes in the traditional heat-driven reactions.^[39,47] Light can also enhance the surface reactions through the photothermal effect only with a very strong intensity which is orders of magnitude higher than that of sunlight.^[40,48,49] Several simple experimental procedures, such as analyzing the dependence of photocatalytic activity on the light intensity and wavelength, have been adopted to detect the contribution of the photothermal effect in light-driven reactions.^[50] As a new family of photocatalysts, metal nanoparticles exhibit fundamentally different behavior compared with the traditional semiconductor photocatalysts.^[51] This comes from the fact that metal possesses a continuous energy structure while semiconductor has a band gap.^[52,53] For the photocatalytic reactions on metal nanoparticles driven by light-induced energetic charge carriers, positive dependence of quantum efficiency and reaction rate on light intensity and temperature has been observed.^[42,43,51,54] While for the photocatalytic reactions on semiconductors, higher light intensity generally leads to lower quantum efficiency, and higher temperature will cause an increased rate of electron-hole pair recombination and thus restrict the surface reactions.^[55,56] Therefore,

the ability to effectively couple thermal and photonic stimuli to drive chemical transformations makes metal nanoparticles superior to the conventional semiconductor photocatalysts in solar-to-chemical conversion.^[47,51,57] Another advantage of metal nanoparticle photocatalysts over semiconductor photocatalysts is the reaction process can be tuned on metal nanoparticles by varying the photoexcitation energy rather than be strongly restricted by the energy gaps of semiconductors.^[45,47,53] Light-driven chemical transformations on metal nanoparticles originate from the light absorption by metal nanoparticles either through the localized surface plasmon resonance (LSPR) or interband transitions.^[42,54] Photoexcitation with whichever absorption mode (plasmon excitation or interband excitation) generates energetic charge carriers (hot electrons), which will migrate to the lowest unoccupied molecular orbitals of the adsorbed molecules to activate chemical bonds and induce surface reactions if the hot electrons have sufficient energy (Scheme S2A).^[42,46] Nevertheless, when strong chemisorption of molecules on the metal surface occurs, the hybridization of the molecular orbitals and the metal orbitals will generate different highest occupied molecular orbitals (HOMO) and lowest unoccupied molecular orbitals (LUMO). This will facilitate the light absorption by the direct photoexcitation which excites the electrons at the HOMO level into the LUMO level and activate chemical bonds to induce surface reactions (Scheme S2B).^[42,46] An experimental signature of the light-driven reactions initiated by the direct photoexcitation of electrons in the hybrid orbitals is the unusual action spectrum where the light enhanced activities at different wavelengths do not follow the light absorption spectrum of the metal nanoparticles.^[58] This is a useful tool to distinguish the direct photoexcitation from the more commonly observed indirect photoexcitation.



Scheme S2. Sketches of different photoexcitation modes of light-driven chemical transformations on metal nanoparticles: (A) light absorption by metal nanoparticles and indirect photoexcitation and (B) light absorption by a metal-adsorbate complex through direct photoexcitation.^[42,46]

Among various transition metals, the three coinage metals, Au, Ag, and Cu, exhibit obvious LSPR in the visible range and are typically regarded as the plasmonic metals.^[39] Other transition metals, such as Pt, Pd, and Ni, are non-plasmonic metals. LSPR is a typical intraband transitions, which are accessible with visible light photons for all transition metals. For the plasmonic metal, the *d* band lies below the Fermi level (E_f), and only high-energy photons can induce interband *d*-to-*s* excitations for these metals (Scheme S3A).^[39] Ag has a full *d* band that lies well below the Fermi level and *d*-to-*s* interband excitations cannot occur in Ag under visible light. While for Au and Cu, the energy of the *d* band is higher compared with Ag, and visible light photons above a specific threshold energy are able to induce *d*-to-*s* interband excitations. Therefore, for the visible-light-driven chemical transformations on Au and Cu nanoparticles, interband transitions will play a non-negligible role in addition to plasmonic excitation.^[54] In the case of non-plasmonic metals, the *d* band is not completely full and intersects the Fermi level (Scheme S3B) allowing for *d*-to-*s* interband excitations to occur throughout the UV-visible range.^[39,54] The interband transitions in the non-plasmonic metals strongly damp the LSPR effect and broaden the LSPR absorption band of these metals.^[54] Therefore, for the visible-light-driven chemical transformations on non-plasmonic nanoparticles, interband transitions are expected to play the dominant role.^[57,59]



Scheme S3. Sketches of the representative density of states of a plasmonic metal (A) and non-plasmonic transition metal (B).^[39]

LSPR is a strong light-matter interaction which allows the plasmonic metal nanoparticles to concentrate the light energy near their surface.^[54,60] Plasmonic Au, Ag, and Cu nanoparticles or multicomponent plasmonic nanocatalysts which contain at least one of the plasmonic metal as light absorption antenna are the most studied photocatalysts for the light-driven chemical transformations.^[61-65] In general, light absorption through interband transitions is weaker than by LSPR. Nevertheless, non-plasmonic Pt group metal nanoparticles have been demonstrated to be effective in driving organic transformations using visible light, such as dehydrogenation, partial oxidation, cross-coupling, and Fischer-Tropsch synthesis reactions.^[57,59] Other than these Pt group metals, the non-plasmonic and non-precious metals, such as Ni, Co, and Fe, are also recognized as industrially important catalysts. However, until now, the use of light irradiation to enhance the efficiency of organic transformations with non-plasmonic and non-precious metal nanoparticles has been largely overlooked. Developing photocatalysts using these metals will obviously expand the field of green photocatalysis and help to achieve theoretical breakthrough in the uncovered light-driven mechanism on non-plasmonic and non-precious metal nanoparticles.

For more information on the underlying physical mechanisms, plasmonic and nonplasmonic photocatalysts, catalysis applications, and outlook of this hot topic, please refer to some of the excellent reviews.^[39,42,43,50,54,60,61,62,66]

2. Experimental Procedures

Materials and chemicals. Zirconium(IV) oxide nanopowder (ZrO_2 , < 100 nm), nickel(II) nitrate hexahydrate ($\text{Ni}(\text{NO}_3)_2 \cdot 6\text{H}_2\text{O}$, $\geq 98.5\%$), sodium borohydride (NaBH_4 , $\geq 98.0\%$), anhydrous 2-butanol (99.5%), benzyl phenyl ether (98%), diphenyl ether (99%), anhydrous benzene ($\geq 99.0\%$), anhydrous toluene (99.8%), anhydrous ethylbenzene (99.8%), acetophenone ($\geq 99\%$), 1-phenylethanol (98%), phenol ($\geq 99\%$), cyclohexanol (99%), 5,5-Dimethyl-1-pyrroline-*N*-oxide (DMPO), phenyl-*N-tert*-butylnitron (PBN, $\geq 98\%$), and anhydrous *n*-decane ($\geq 99\%$) were purchased from Sigma-Aldrich. 2-Phenylethyl phenyl ether ($\geq 95\%$), 2-(2-methoxyphenoxy)-1-(4-methoxyphenyl)propane-1,3-diol (97%), and 1-(4-hydroxy-3,5-dimethoxyphenyl)-2-(2-methoxyphenoxy)propane-1,3-diol (96%) were purchased from Ark Pharm, Inc. (USA). 2-Phenoxy-1-phenylethanol (98%), 2-phenoxy-1-phenylethanone ($> 98.0\%$), anhydrous ruthenium(III) chloride (RuCl_3 , Ru content 45-55%), chloroplatinic acid hexahydrate ($\text{H}_2\text{PtCl}_6 \cdot 6\text{H}_2\text{O}$, AR, Pt $\geq 37.5\%$), and palladium chloride (PdCl_2 , 99.999% metals basis) were purchased from Aladdin (Shanghai, China). Ammonium sulfate ($(\text{NH}_4)_2\text{SO}_4$, AR, $\geq 99.0\%$), hydrazine hydrate ($\text{N}_2\text{H}_4 \cdot \text{H}_2\text{O}$, AR, $\geq 80\%$), anhydrous methanol (AR, $\geq 99.5\%$), anhydrous ethanol ($\geq 99.8\%$), isopropanol (AR), *n*-butanol (AR), and isobutanol (AR) were provided by Beijing Chemical Works (China). 1-(4-Hydroxy-3-methoxyphenyl)-2-(2-methoxyphenoxy)propane-1,3-diol ($> 97.0\%$) and dealkaline lignin (Product No. L0045) was purchased from TCI Chemicals. Deionized water was used throughout the experiments. All the chemicals were used without further purification.

Synthesis of catalysts. ZrO_2 supported Ni nanocatalysts (Ni/ZrO_2 , 9.09 wt.%) were prepared by an impregnation-reduction method. 1.0 g ZrO_2 nanopowder was dispersed into 50 mL aqueous solution of $\text{Ni}(\text{NO}_3)_2 \cdot 6\text{H}_2\text{O}$ ($0.034 \text{ mol} \cdot \text{L}^{-1}$) with magnetic stirring at room temperature for 30 min. 10 mL of freshly prepared NaBH_4 aqueous solution ($1.75 \text{ mol} \cdot \text{L}^{-1}$) was added dropwise in 20 min. After stirred for another 30 min, the suspension was allowed to age overnight. Then, the wet catalyst was separated by centrifugation (6000 rpm, 5 min), washed with deionized water (three times) and anhydrous ethanol (once), and finally dried at 40°C under vacuum for 24 h. Finally, the dried catalyst was reduced in flowing H_2 :Ar (1:9, v/v) mixture ($200 \text{ mL} \cdot \text{min}^{-1}$) for 0.5 h at 600°C at a heating ramp of $10^\circ\text{C} \cdot \text{min}^{-1}$. Reducing temperatures of 400, 500, 700, and 800°C were also used and these resulting catalysts were denoted as Ni/ZrO_2 (T) according to the reducing temperature. ZrO_2 supported Ru, Pd, and Pt nanocatalysts (Ru/ZrO_2 , Pd/ZrO_2 , Pt/ZrO_2 , 9.09 wt.%) were also synthesized by the similar impregnation-reduction method without thermal reducing by H_2 using their respective metal precursors.

Characterization of catalysts. The exact Ni content of Ni/ZrO_2 catalysts was determined on an Agilent 725 inductively coupled plasma optical emission spectrometer (ICP-OES). To obtain dissolved samples, Ni/ZrO_2 catalysts were mixed with concentrated H_2SO_4 (98%) and $(\text{NH}_4)_2\text{SO}_4$ in a 150 mL PTFE lined hydrothermal autoclave reactor and heated at 180°C for 10 h.

The fraction of Ni metal in Ni/ZrO_2 catalysts ($F_{\text{Ni}(0)}$) was determined by H_2 temperature-programmed reduction (H_2 -TPR) method^[67] on a Micrometric AutoChem II 2920 chemisorption instrument. About 100 mg of unreduced Ni/ZrO_2 or reduced Ni/ZrO_2 (T) catalysts were sealed in a quartz tube reactor and pretreated under Ar atmosphere at 300°C for 1 h. After cooled down to 50°C , H_2 -TPR was conducted in flowing H_2 :Ar (1:9, v/v) mixture ($300 \text{ mL} \cdot \text{min}^{-1}$) to $900 \text{ mL} \cdot \text{min}^{-1}$ at a heating ramp of $10^\circ\text{C} \cdot \text{min}^{-1}$. The amount of H_2 consumed was recorded by the equipped thermal conductivity detector (TCD). The fraction of Ni metal in each Ni/ZrO_2 catalyst was calculated based on the amount of H_2 consumed by

$$F_{\text{Ni}(0)} = \frac{C_{\text{H-total}} - C_{\text{H}}}{C_{\text{H-total}}} \times 100\%$$

where $C_{\text{H-total}}$, C_{H} are the total H_2 consumption of the unreduced Ni/ZrO_2 sample and the H_2 consumption of the reduced Ni/ZrO_2 catalyst, respectively.

The surface Ni chemical state of Ni/ZrO_2 catalysts was analyzed by X-ray photoelectron spectroscopy (XPS) on a Thermo ESCALAB 250Xi instrument with a monochromatized Al K α line source. The energy scales of all spectra were calibrated using the C 1s level at the binding energy of 284.8 eV as a reference. By quantitatively analyzing the surface nickel chemical states, the fraction of Ni metal at the surface ($F_{\text{Ni}(0-s)}$) of each reduced Ni/ZrO_2 catalyst can be obtained.

The particle size and morphology of Ni/ZrO_2 catalysts were characterized on a FEI Tecnai G2 F20 field emission transmission electron microscope (FE-TEM). The theoretical dispersion of metal Ni (D , %) can be estimated using the Ni particle size (d , nm) measured from TEM images, based on spherical model^[68,69]:

$$D = \frac{6M}{d \cdot N_A \cdot \rho \cdot \sigma} \times 100\%$$

where M is the molecular weight of Ni, N_A is the Avogadro's number, ρ is the metal density of Ni, σ is the atomic cross-sectional area of Ni which equals to 6.494 \AA^2 . This equation is simplified to $D (\%) = 101/d$ (nm), by substituting these values.

The absorption spectra of Ni/ZrO_2 catalysts were collected on a Varian Cary 5000 spectrometer (with UV-3150 UV-Vis spectrophotometer equipped with an integrating sphere using BaSO_4 as the reference).

Photocatalytic reactions. Scheme S4 presents the experimental setups. A 10 mL borosilicate glass tube ($\phi = 16 \text{ mm}$, ASONE) was used as the reaction container. In a typical reaction, after being charged with the photocatalyst (20 mg), reactant (0.05 mmol), additive (hydrazine hydrate 0.05 mmol, 1 equiv.), and solvent (2 mL), the tube was filled with argon and sealed with a polypropylene screw cap with a silicone gasket. Then the reaction mixture was stirred magnetically and irradiated by a PerfectLight PLS-LED100B LED light source (spectral output in the range of 400-800 nm, Figure S1) to conduct the photocatalytic reactions. The reaction

temperature was carefully controlled in an oil bath by a Shanghai Sile S10-3 magnetic stirrer with heating module. For these reactions which were conducted at room temperature (no external heating), the reaction temperature fluctuated slightly during the reaction as recorded on a FLIR E4 thermal camera (Figure S2). Photocatalytic action spectrum was obtained by carrying out reactions at several specific wavelengths using a 300 W Xenon lamp (CEL-HXF300, Beijing China Education Au-light Co., Ltd.) equipped with several monochromatic filters. The photocatalytic hydrogenolysis of PP-ol was also conducted using sunlight directly at ambient condition on a Kylin-Bell TS-100 horizontal shaker in late July in Beijing where temperature was 32-35 °C, solar irradiation intensity on the reactor surface was 32-40 mW·cm². All the dark reactions were carried out with the tube wrapped with aluminum foil to avoid exposure of the reaction to light while other conditions maintained identical. Initial reaction rate (*r*) was determined by controlling the reaction conditions to obtain a conversion of below 30%. All the reactions were carried out at least three times to obtain the reproducible results. For photocatalyst recycling experiments, after each cycle, the tested photocatalyst was collected by centrifugation, washed thoroughly with anhydrous ethanol twice, dried at 40 °C under vacuum, and then reduced at 600 °C for 0.5 h for the subsequent reaction.

After a certain time, 0.5 mL of the reaction solution was collected and then filtered through a Millipore filter (0.45 μm) to remove the solid photocatalyst particulates. The products were identified by a Shimadzu GCMS-QP2010 instrument and were quantitatively analyzed on a Shimadzu GC-2014C gas chromatography using external standard method. Conversion is defined as the amount of reactant converted during the reaction divided by the total amount of the reactant, multiplied by 100%. Selectivity and yield of a specific product presented are based on the number of C atoms,^[12] unless otherwise specified. Selectivity is defined as the number of C atoms in the product of interest divided by the total number of C atoms in the products, multiplied by 100%, and yield is defined as the number of C atoms in the product of interest divided by the number of C atoms in the reactant, multiplied by 100%. Turnover frequency (TOF) is defined as the converted reactants per mol of surface Ni active site per hour, unless otherwise specified. The amount of surface Ni active sites is determined based on Ni dispersion (*D*) and the fraction of Ni metal at the surface (*F_{Ni(0-S)}*). The apparent activation energy (*E_a*) of each reaction can be obtained using the Arrhenius equation:

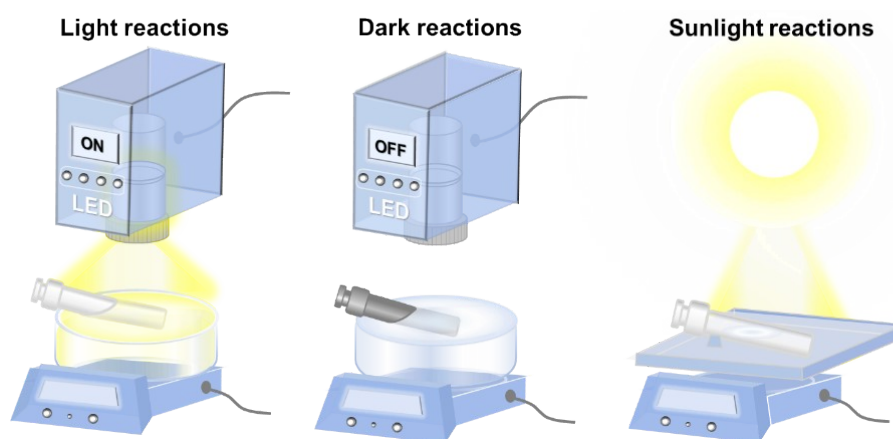
$$K = A \cdot \exp\left(-\frac{E_a}{R \cdot T}\right)$$

where *K* is the rate constant which is expressed as the initial TOF in this study, *A* is pre-exponential constant factor, *R* is the gas constant, and *T* is the absolute temperature.

The photocatalytic apparent quantum efficiency (AQE) is defined as the number of converted reactant molecules induced by light per unit time per incident photon,^[47] which can be expressed as

$$\text{AQE} = \frac{(r_{\text{light}} - r_{\text{dark}}) \cdot N_A \cdot h \cdot c}{I \cdot A \cdot \lambda} \times 100\%$$

where *r_{light}* and *r_{dark}* are the initial rates of light and dark reactions, respectively, *N_A* is Avogadro's constant, *h* is Planck's constant, *c* is the speed of light in vacuum, *I* is the intensity of the monochromatic light, *A* is the irradiation area, which is equal to 2.95 × 10⁻⁴ m², and *λ* is the wavelength of the monochromatic light.



Scheme S4. Experimental setups of light, dark, and sunlight reactions.

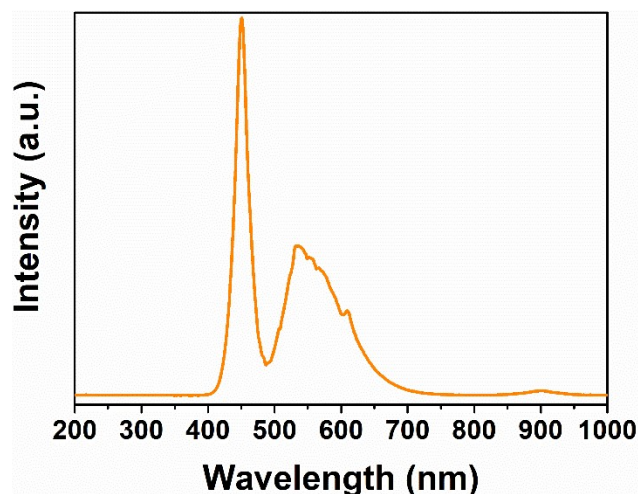


Figure S1. The output spectral distribution of the LED light source.

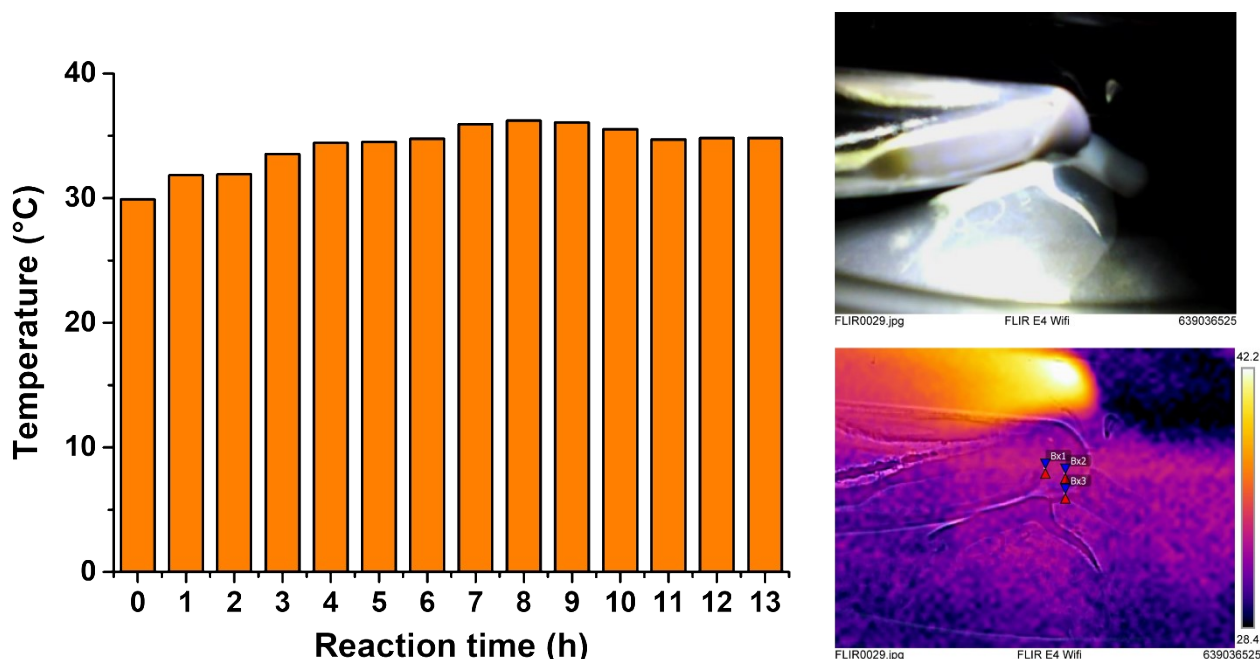


Figure S2. Temperature fluctuation recorded on a thermal camera during the hydrogenolysis of BPE catalyzed by Ni/ZrO₂ (Table S3, Entry 5). The images obtained at the beginning of the reaction are also given as examples. The presented temperature value of each timepoint is the average value of three test points as shown in the thermal image (Bx1, Bx2, Bx3).

Photocatalytic cleavage of complex β -O-4 model compounds. Three complex β -O-4 model compounds, 2-(2-methoxyphenoxy)-1-(4-methoxyphenyl)propane-1,3-diol (MMP), 1-(4-hydroxy-3-methoxyphenyl)-2-(2-methoxyphenoxy)propane-1,3-diol (HMMP), and 1-(4-hydroxy-3,5-dimethoxyphenyl)-2-(2-methoxyphenoxy)propane-1,3-diol (HDMP), were also employed for photocatalytic cleavage study. The reactions were conducted using the same method as described above with the reaction conditions: reactant 0.05 mmol, 2-butanol 2 mL, Ni/ZrO₂ 20 mg, hydrazine hydrate 0.05 mmol (1.0 equiv.), 0.5 W·cm⁻² intensity of LED light. After reaction, 0.5 mL of the reaction solution was collected and then filtered through a Millipore filter (0.45 μ m) to remove the solid photocatalyst particulates. Then, 50 μ L of an internal standard solution (*n*-decane in 2-butanol, 10 mg·mL⁻¹) was added. The aromatic monomer products were identified by GC-MS and quantified by GC-FID based on the internal standard. Yield of a monomer product is defined as the weight of this product divided by the weight of the reactant, multiplied by 100%.

Photocatalytic depolymerization of lignin sample. A commercially available dealkaline lignin sample from TCI Chemicals (Product No. L0045) was used for the photocatalytic depolymerization study. It was prepared by TCI from needle-leaved trees and broad-leaved trees through the treatment of sodium sulfite followed by the chemical modifications such as partial desulfonation, oxidation, hydrolysis and demethylation, as shown at <https://www.tcichemicals.com/IN/en/p/L0045>. Specifications of the dealkaline lignin sample are also provided at this site which contain appearance, methoxyl group, water, ignition residue (sulfate), and pH. It has a high molecular weight and is contaminated with Na and S.^[70,71] Deepa and Dhepe determined the molecular weight of this lignin sample to be 60,000 g·mol⁻¹ (M_n) by MALDI-TOF.^[70] Shu et al. determined the molecular weights of this lignin sample to be 58,449 g·mol⁻¹ (M_n) and 81,776 g·mol⁻¹ (M_w) by GPC.^[a29] They also analyzed the element compositions of this lignin sample and determined its molecular formula to be C₉H_{11.78}O_{6.27}N_{0.03}S_{0.31}Na_{0.48}.^[71] We tried to analyze the structure of this lignin sample on a 500

MHz nuclear magnetic resonance (NMR) spectrometer (Bruker AVANCE III HD500) using the same method reported by Nandiwale et al.^[72] and the two-dimensional (2D) ¹H-¹³C HSQC (heteronuclear single quantum correlation) NMR spectra are given below. The chemical shifts in the region of 3-5 ppm (¹H) and 50-90 ppm (¹³C) are attributed to the β-β, β-O-4, β-5, and α-O-4 interunit linkages in lignin. Within this region, the peaks observed between 3.2-4.2 ppm (¹H) and 56-58 ppm (¹³C) are attributed to the different methoxy linkages of the syringyl and guaiacyl subunits. Other two regions correspond to the aliphatic and aromatic subunits as shown in Figure S3. However, we failed to calculate the relative contents of C9 units and the interunit linkages because some of the typical linkages in lignin are missing. This might happen during the complex chemical treatment processes.

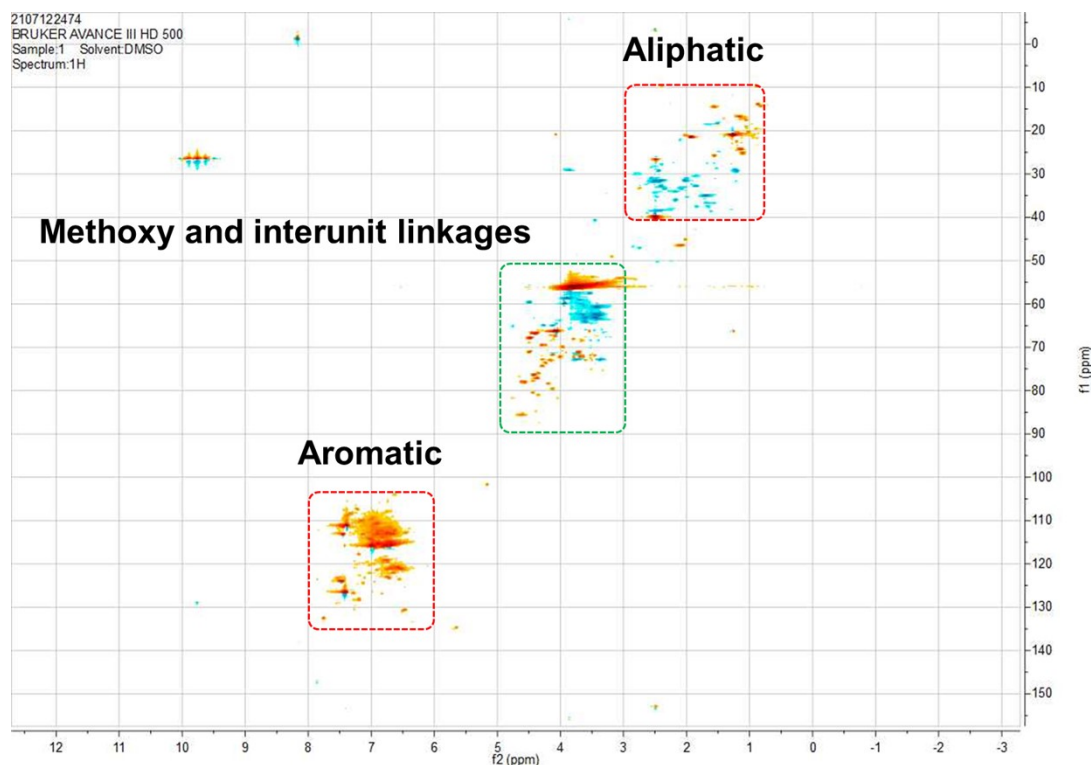


Figure S3. 2D HSQC NMR (DMSO-*d*₆) spectra of dealcaline lignin.

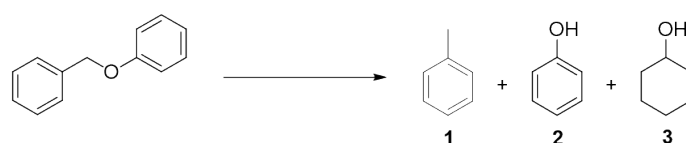
The solubility of the dealcaline lignin sample in water and various hydrogen-donating alcohol solvents (Table S6) was tested using the following procedure: 100 mg of lignin sample was added into 5 mL of the tested solvent, followed by ultrasonic treatment for 20 min and heating at 60 °C for 4 h. After that, the partially dissolved samples were centrifuged to remove the solid, dried at 60 °C for 8 h to remove the solvents, and weighted. Results showed that the lignin sample was fully dissolved in water and methanol, partially dissolved in ethanol (2.01 mg·mL⁻¹), and not dissolved in others. The photocatalytic depolymerization of lignin sample was conducted using the same method as described above. The reaction conditions are: 3 mL solution of lignin in methanol (5 mg·mL⁻¹), 30 mg Ni/ZrO₂ as photocatalyst, 4.5 μL hydrazine hydrate as additive, 0.5 W·cm⁻² intensity of LED light, 80 °C, 35 h. After reaction, the mixture of two sets of parallel reaction was collected and then filtered through a Millipore filter (0.45 μm) to remove the solid photocatalyst particulates. Then the obtained solution was concentrated to about 1 mL. Before analysis, 10 μL of an internal standard solution (*n*-decane in methanol, 10 mg·mL⁻¹) was added. The aromatic monomer products were identified by GC-MS and quantified by GC-FID based on the internal standard (*n*-decane) and the effective carbon number (ECN) method.^[17,73] Yield of a monomer product is defined as the weight of this product divided by the weight of lignin sample, multiplied by 100%.

3. Results and Discussion

3.1. Effect of hydrazine hydrate on the hydrogenolysis of BPE catalyzed by Ni/ZrO₂

We first conducted the hydrogenolysis of BPE without any additives at 60 °C. After 2 h, 98% conversion of BPE and 96% selectivity towards aromatic monomer products, toluene and phenol, was achieved under visible light irradiation (Table S3, Entry 1). However, when this reaction was conducted under dark, only 3% conversion of BPE was observed (Table S3, Entry 2). Then we added 1 equiv. of hydrazine hydrate into this reaction, and found this additive was effective in promoting the activity of Ni/ZrO₂ and enabled this reaction to occur at room temperature (Figure S2) under both visible light and dark conditions (Table S3, Entry 3-6). Control experiments without adding the Ni/ZrO₂ photocatalyst showed no conversion of BPE, illustrating that hydrazine hydrate did not react with BPE directly (Table S3, Entry 7&8). Reducing the amount of hydrazine hydrate to 5 μmol (0.1 equiv.) did not affect the hydrogenolysis of BPE, and sodium borohydride was more effective than hydrazine hydrate as less time was needed to obtain the similar conversion of BPE when sodium borohydride was added (Table S3, Entry 9-12). Further kinetics study in the presence of different amounts of hydrazine hydrate showed that the reaction progress was not affected when the amount of hydrazine hydrate ranging from 5 μmol (0.1 equiv.) to 0.1 mmol (2.0 equiv.) (Figure S4).

Table S3. Effects of additives on the hydrogenolysis of BPE catalyzed by Ni/ZrO₂.



Entry	Reaction conditions ^a			Additive	Conversion (%)	Selectivity (%)		
	Temperature (°C)	Time (h)	Light condition			1	2	3
1	60	2	Visible light	None	98	55	41	4
2			Dark		3	54	46	0
3	r.t.	13	Visible light	None	0	N.D. ^b	N.D.	N.D.
4			Dark		0	N.D.	N.D.	N.D.
5	r.t.	13	Visible light	N ₂ H ₄ ·H ₂ O, 0.05 mmol (1.0 equiv.)	99	54	43	3
6			Dark		30	55	45	0
7 ^c	r.t.	13	Visible light	N ₂ H ₄ ·H ₂ O, 0.05 mmol (1.0 equiv.)	0	N.D.	N.D.	N.D.
8 ^c			Dark		0	N.D.	N.D.	N.D.
9	r.t.	12	Visible light	N ₂ H ₄ ·H ₂ O, 5 μmol (0.1 equiv.)	99	54	43	3
10			Dark		27	54	46	0
11	r.t.	4	Visible light	NaBH ₄ , 5 μmol (0.1 equiv.)	95	55	41	4
12			Dark		50	56	43	1

^aOther conditions: BPE 0.05 mmol, 2-butanol 2 mL, Ni/ZrO₂ 20 mg, 0.5 W·cm⁻² intensity of LED light.

^bN.D. = Not detected.

^cControl experiments without adding Ni/ZrO₂.

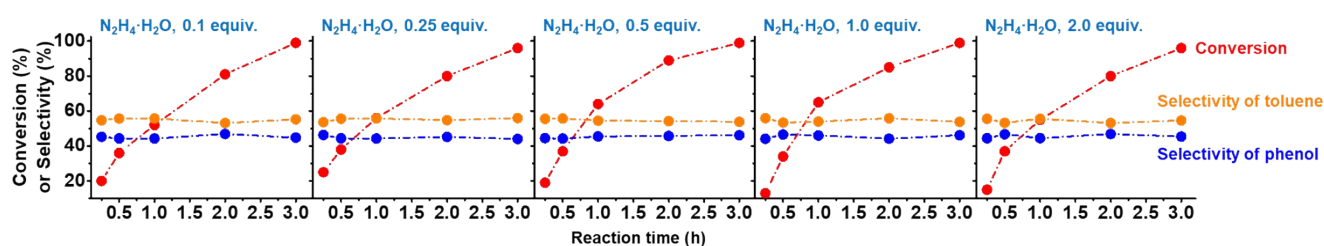


Figure S4. Kinetics profiles for the hydrogenolysis of BPE catalyzed by Ni/ZrO₂ using different amount of hydrazine hydrate. Reaction conditions: BPE 0.05 mmol, 2-butanol 2 mL, Ni/ZrO₂ 20 mg, 0.3 W·cm⁻² intensity of LED light, 50 °C.

The above results suggest that the two commonly used reducing agents, hydrazine hydrate and sodium borohydride can remove oxygen to generate reactive metal surface.^[74] To study the effect of hydrazine hydrate on the properties of the Ni/ZrO₂, we conducted XPS, UV-vis absorption, and H₂-TPR characterizations. The treatment conditions are given in Table S4 and Ni2p_{3/2} spectra and UV-vis absorption spectra are shown in Figure S5. As shown in Figure S5A, the spectra of the four sample treated with hydrazine hydrate (4[#], 5[#], 8[#], 9[#]) present an enhanced band at about 852 eV when compared with the spectra of the original Ni/ZrO₂ sample (0[#]). Further calculating the fraction of Ni metal at surface showed that the amount of metallic Ni increased obviously after the treatment with hydrazine hydrate (Table S4). As metallic Ni serves as the active site for the hydrogenolysis of BPE (see Figure 1), adding hydrazine hydrate into the reaction mixture will increase the amount of active site and accelerate the reaction. The average diameter of Ni nanoparticles was 6.4 nm (Figure S5d) and the exact Ni content of Ni/ZrO₂ was determined to be 8.66 ± 0.14 wt.% by ICP-OES, the theoretical amount of surface Ni was calculate to be 4.7 μmol based on spherical mode^[68,69]. Therefore, 0.1 equiv. of hydrazine hydrate was sufficient to activate these surface Ni sites during the reaction (Figure S4). Neither inducing visible light nor increasing reaction temperature activated the surface of Ni as hydrazine hydrate did (Table S4). However, both visible light and higher temperature enhanced the photocatalytic performance (Table S3). This is because Ni nanoparticles can effectively couple thermal and light stimuli to drive chemical transformations, as we demonstrated in the introduction and light-driven mechanism sections. Furthermore, H₂-TPR analysis showed that the fraction of Ni metal in bulk was not affected by the treatment with hydrazine hydrate (Table S4). The light absorption property of the Ni/ZrO₂ catalyst was also not affected during the reaction as shown in Figure S5B.

Table S4. The fraction of Ni metal in the Ni/ZrO₂ catalyst treated by hydrazine hydrate.^a

Entry	Sample number	Treatment conditions				$F_{Ni(O)-S}$ determined by XPS ^b	$F_{Ni(O)}$ determined by H ₂ -TPR
		Temperature (°C)	Time (h)	Light condition	Additive		
1 ^c	0 [#]	-	-	-	-	40.56	94.55
2	1 [#]	r.t.	2	Visible light	None	36.02	95.04
3	2 [#]			Dark		34.29	94.22
4	3 [#]	r.t.	2	Visible light	N ₂ H ₄ ·H ₂ O, 0.05 mmol (1.0 equiv.)	55.55	94.32
5	4 [#]			Dark		52.01	93.78
6	5 [#]	60	0.5	Visible light	None	36.22	95.28
7	6 [#]			Dark		35.83	93.92
8	7 [#]	60	0.5	Visible light	N ₂ H ₄ ·H ₂ O, 0.05 mmol (1.0 equiv.)	56.88	95.31
9	8 [#]			Dark		55.12	94.63

^aThe fraction of Ni metal in various Ni/ZrO₂ catalysts in bulk and at surface was determined by H₂-TPR and XPS, respectively.

^bThe Ni/ZrO₂ samples for XPS analysis were protected by Ar throughout the treatment and sample preparation processes in an anaerobic glovebox.

^cThe 0[#] sample is the original Ni/ZrO₂ catalyst without any treatment.

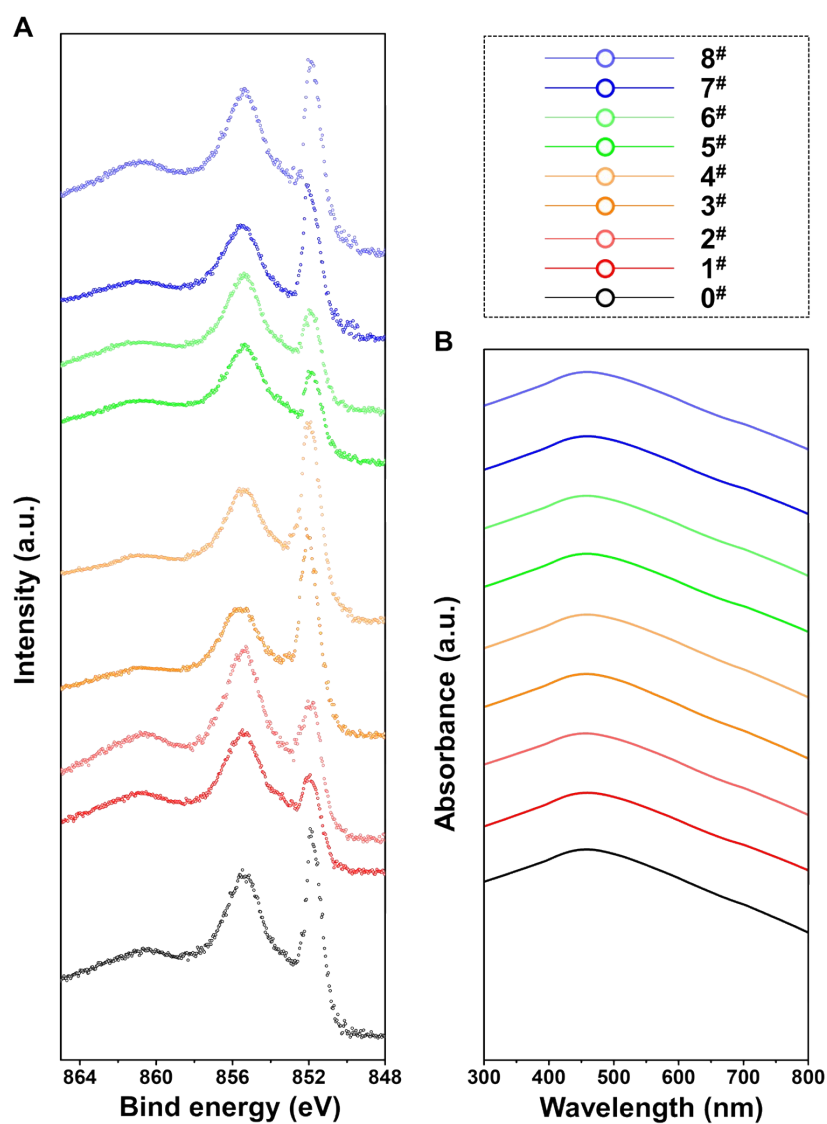


Figure S5. Characterization of the Ni/ZrO₂ catalyst treated by hydrazine hydrate: (A) Ni2p_{3/2} spectra and (B) UV-vis absorption spectra of Ni/ZrO₂ dispersed in 2-butanol (5 mg catalyst in 20 mL solvent). The treatment conditions for each sample are given in Table S4.

3.2. Photocatalytic hydrogenolysis of BPE by various catalysts

Other than Ni, ZrO₂ supported nanocatalysts of Ru, Pt, and Pd were also tested for the hydrogenolysis of BPE. As shown in Table S5, Ru/ZrO₂ and Pt/ZrO₂ were also active for this reaction, although longer reaction time was used for Ru/ZrO₂ and both higher temperature and longer time were used for Pt/ZrO₂ than these for Ni/ZrO₂ to obtain similar performance as Ni/ZrO₂ under visible light. Moreover, both Ru/ZrO₂ and Pt/ZrO₂ showed visible light enhanced activity due to their interaction with visible light energy through interband transitions.^[57] Then we studied the effect of oxygen gas on the activity of Ru/ZrO₂ and Ni/ZrO₂ by replacing argon by air. Results showed that Ni/ZrO₂ was sensitive to oxygen and no reaction took place under air while Ru/ZrO₂ was more resistance to oxygen with its catalytic performance less affected. We also studied the effect of hydrazine hydrate on the activity of Ru/ZrO₂ and a moderate inhibition effect rather than promotion effect as in the case of Ni/ZrO₂ was observed. This is because Ru nanoparticles were different from Ni nanoparticles which were always covered by a thin oxide layer, and hydrazine hydrate would not activate Ru during the reaction.

Table S5. Performance of various catalysts for the photocatalytic hydrogenolysis of BPE.



Entry	Catalysts	Reaction conditions ^a				Conversion (%)	Selectivity (%)				
		Temperature (°C)	Time (h)	Atmosphere	Light condition		1	2	3		
1	Ni/ZrO ₂	60	2	Ar	Visible light	98	55	41	4		
2					Dark	3	54	46	0		
3				Air	Visible light	0	N.D. ^b	N.D.	N.D.		
4					Dark	0	N.D.	N.D.	N.D.		
5	Ru/ZrO ₂	60	2	Ar	Visible light	47	56	30	14		
6					Dark	30	55	41	4		
7				Air	Visible light	40	56	31	13		
8					Dark	22	55	45	0		
9 ^c				60	7	Ar	Visible light	35	55	34	11
10 ^c							Dark	14	54	42	4
11							Visible light	98	56	26	18
12							Dark	52	56	32	12
13	Pt/ZrO ₂	60	2	Ar	Visible light	0	N.D.	N.D.	N.D.		
14					Dark	0	N.D.	N.D.	N.D.		
15				80	7	Visible light	99	55	42	3	
16						Dark	36	56	44	0	
17	Pd/ZrO ₂	60	2	Ar	Visible light	0	N.D.	N.D.	N.D.		
18					Dark	0	N.D.	N.D.	N.D.		
19					80	7	Visible light	0	N.D.	N.D.	N.D.
20							Dark	0	N.D.	N.D.	N.D.

^aOther conditions: BPE 0.05 mmol, 2-butanol 2 mL, catalyst 20 mg, 0.5 W·cm⁻² intensity of LED light.

^bN.D. = Not detected.

^cHydrazine hydrate (0.05 mmol, 1.0 equiv.) was added.

3.3. Photocatalytic hydrogenolysis of BPE in various solvents

Various alcohol solvents were employed as hydrogen-donating solvents for the hydrogenolysis of BPE catalyzed by Ni/ZrO₂.^[34,75] As shown in Table S6, other than 2-butanol, isopropanol was also an efficient solvent for this reaction. In isopropanol, the hydrogenolysis occurred at room temperature under visible light irradiation, but the conversion of BPE obtained in it was lower than that obtained in 2-butanol at the same conditions. In other solvents, this reaction could not happen at room temperature. When achieving similar conversion of BPE as in isopropanol (~30%), 70 °C and 7 h were needed in isobutanol, 80 °C and 12 h were needed in ethanol, 80 °C and 24 h were needed in *n*-butanol. Methanol was the least efficient solvent among them as the conversion of BPE in methanol was only 5% at 90 °C for 24 h. In summary, the efficiency of these hydrogen-donating solvents for this reaction decreases in the order 2-butanol > isopropanol > isobutanol > ethanol > *n*-butanol > methanol.

Table S6. Photocatalytic hydrogenolysis of BPE by Ni/ZrO₂ in various alcohol solvents.



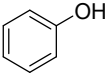
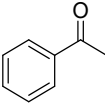
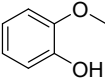
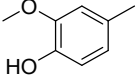
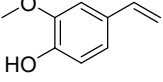
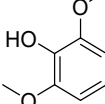
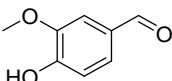
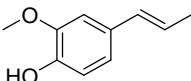
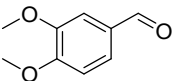
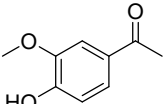
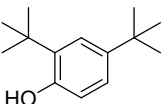
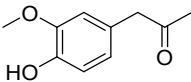
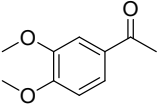
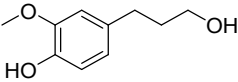
Entry	Solvents	Reaction conditions ^a			Conversion (%)	Selectivity (%)		
		Temperature (°C)	Time (h)	Light condition		1	2	3
1	Methanol	90	24	Visible light	5	58	42	0
2				Dark	0	N.D. ^b	N.D.	N.D.
3	Ethanol	80	12	Visible light	29	48	52	0
4				Dark	0	N.D.	N.D.	N.D.
5	Isopropanol	r.t.	13	Visible light	30	48	52	0
6				Dark	0	N.D.	N.D.	N.D.
7	<i>n</i> -Butanol	80	24	Visible light	28	55	44	1
8				Dark	0	N.D.	N.D.	N.D.
9	2-Butanol	r.t.	13	Visible light	99	54	43	3
10				Dark	30	55	45	0
11	Isobutanol	70	7	Visible light	29	47	53	0
12				Dark	10	48	52	0

^aOther conditions: BPE 0.05 mmol, solvent 2 mL, Ni/ZrO₂ 20 mg, hydrazine hydrate 0.05 mmol (1.0 equiv.), 0.5 W·cm⁻² intensity of LED light.

^bN.D. = Not detected.

3.4. Quantification of the identified aromatic monomers from the photocatalytic depolymerization of dealkaline lignin

Table S7. Identified aromatic monomer products from the photocatalytic depolymerization of dealkaline lignin.

Monomer number	Retention time (min)	Monomer structure	Systematic name	CAS number	ECN	Yield (wt.%)
1	7.295		Phenol	108-95-2	5	0.43
2	8.790		1-Phenylethanone	98-62-2	7.25	0.22
3	9.036		2-Methoxyphenol	90-05-1	5	3.09
4	10.584		2-Methoxy-4-methylphenol	93-51-6	6	0.15
5	12.356		2-Methoxy-4-vinylphenol	7786-61-0	7.15	0.14
6	12.814		2,6-Dimethoxyphenol	91-10-1	5	0.07
7	13.552		4-Hydroxy-3-methoxybenzaldehyde	121-33-5	5	3.47
8	14.218		2-Methoxy-4-(1-propenyl)-phenol	97-54-1	8.25	0.23
9	14.536		3,4-Dimethoxybenzaldehyde	120-14-9	6	0.12
10	14.684		1-(4-Hydroxy-3-methoxyphenyl)ethanone	498-02-2	6.25	1.16
11	14.881		2,4-Bis(2-methyl-2-propanyl)phenol	96-76-4	13	0.05
12	15.189		1-(4-Hydroxy-3-methoxyphenyl)acetone	2503-46-0	7.25	0.14
13	15.579		1-(3,4-Dimethoxyphenyl)ethanone	1131-62-0	7.25	0.07
14	16.656		4-(3-Hydroxypropyl)-2-methoxyphenol	2305-13-7	7.4	0.50

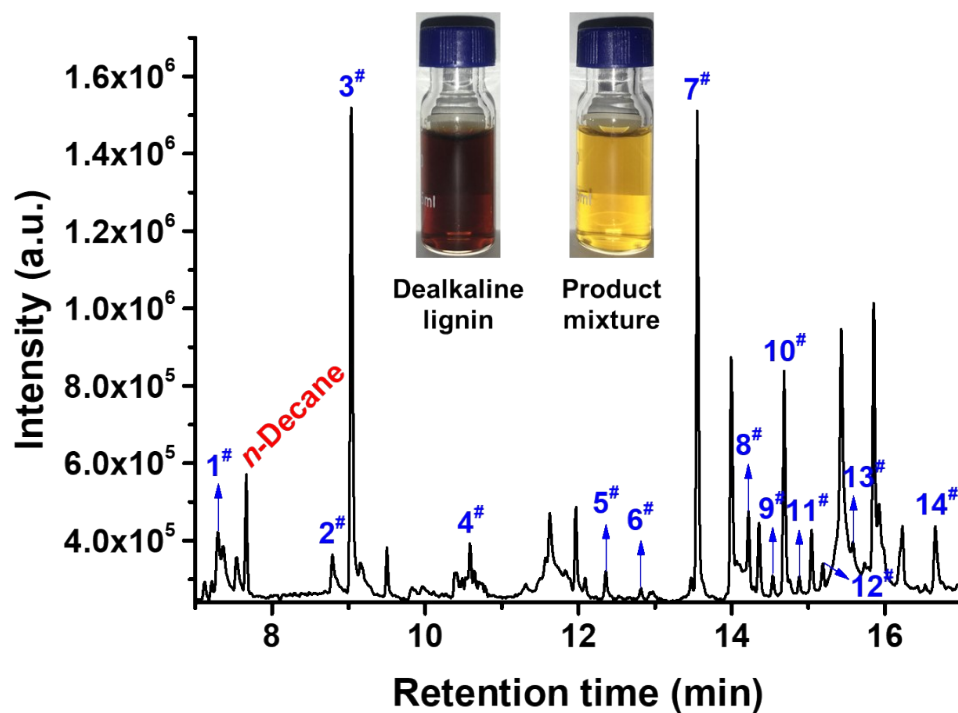


Figure S6. GC analysis of the obtained product mixture from the photocatalytic depolymerization of dealkaline lignin showing the identified monomers with the inserted photographs of the dealkaline lignin solution and the product mixture.

3.5. Characterization of Ni/ZrO₂ catalysts

These Ni/ZrO₂ catalysts which were thermally reduced by H₂ at different temperatures as well as the unreduced Ni/ZrO₂ catalyst were characterized by several techniques. Firstly, the particle size and morphology of ZrO₂ supported Ni nanoparticles were characterized by TEM with the results given in Figure S7. In the TEM image of the unreduced Ni/ZrO₂ catalyst, no Ni nanoparticles but amorphous Ni species were observed. After the thermal reducing treatment with flowing H₂ gas, Ni nanoparticles of quasi-spherical morphology formed and uniformly dispersed on ZrO₂ support. The particle size distribution of Ni nanoparticles was measured based on the obtained TEM images using ImageJ, which is an open source Java image processing program inspired by NIH Image.^[76] As shown in Figure S7, the obtained Ni nanoparticles in all the five reduced samples had a narrow size distribution.^[77] The average particle size of each catalyst was also provided in Figure S7, which illustrated that a reducing temperature higher than 700 °C would cause obvious particle size increase of Ni nanoparticles.

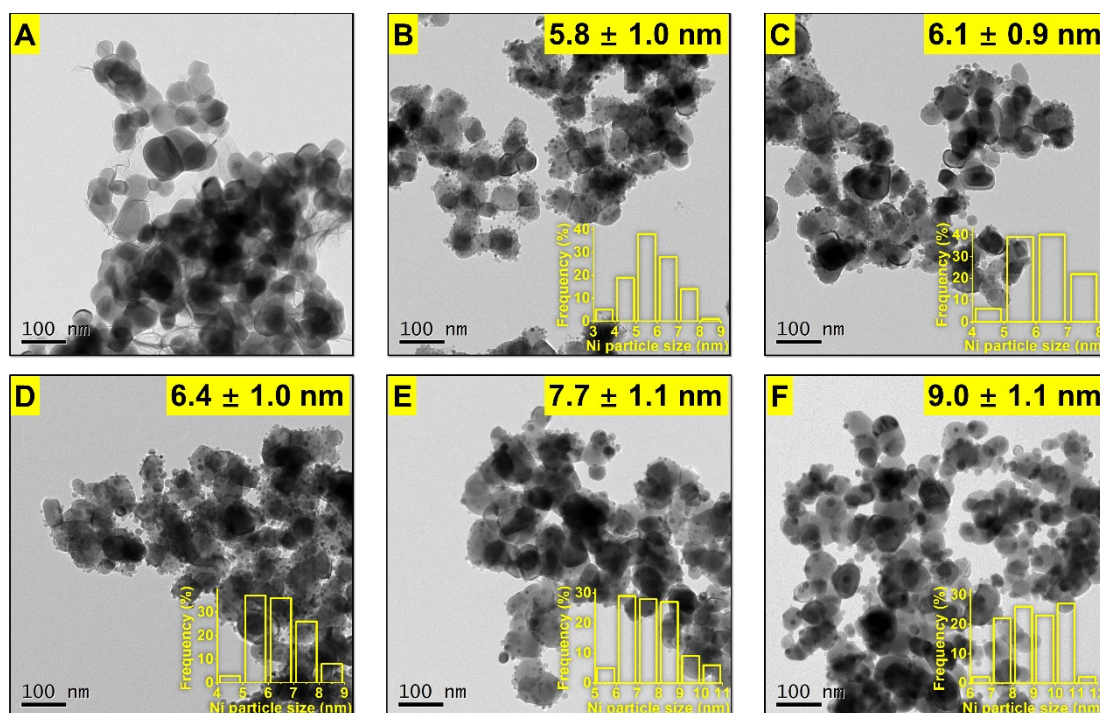


Figure S7. TEM images of Ni/ZrO₂ catalysts with the inserted histogram of size distribution of Ni nanoparticles: (A) Ni/ZrO₂ (unreduced), (B) Ni/ZrO₂ (400), (C) Ni/ZrO₂ (500), (D) Ni/ZrO₂ (600), (E) Ni/ZrO₂ (700), (F) Ni/ZrO₂ (800).

The fraction of Ni metal in various Ni/ZrO₂ catalysts in bulk and at surface was determined by H₂-TPR and XPS, respectively. H₂-TPR profiles of Ni/ZrO₂ catalysts together with the calculated fraction of Ni metal were presented in Figure S8. The TPR profile of the unreduced Ni/ZrO₂ catalyst showed a complex H₂ consumption band ranging from 200 to 600 °C which was ascribed to the reducing of different Ni species in oxidation states.^[78] The intensity of this band decreased gradually with raising the reducing temperature of Ni/ZrO₂ catalysts from 400 to 600 °C. When the reducing temperature reached 600 °C, a nearly complete reducing of Ni was obtained. Further raising the temperature did not increase the fraction of Ni metal, which maintained at about 90% with the reducing temperature in the range of 600-800 °C. As a surface sensitive technique, XPS was used to analyze the surface Ni chemical state in the reduced Ni/ZrO₂ catalysts. Ni2p_{3/2} spectra of the reduced Ni/ZrO₂ catalysts show an extra band at about 852.5 eV when compared with that of the unreduced Ni/ZrO₂ catalyst (Figure S9A), illustrating the formation of metallic Ni by the thermal reducing effect of H₂.^[79] In order to determine the fraction of Ni metal at the surface of each reduced Ni/ZrO₂ catalyst, the fitting procedures proposed by Biesinger et al. was employed to quantitatively analyze the mixed nickel chemical states.^[80] One specific example of Ni/ZrO₂ (600) was given in Figure S9B illustrating the presence of metallic Ni, NiOOH, NiO, and Ni(OH)₂ which possibly formed when the nickel catalyst exposed to air.^[81] $F_{Ni(0)-S}$ of Ni/ZrO₂ (400), Ni/ZrO₂ (500), Ni/ZrO₂ (600), Ni/ZrO₂ (700), and Ni/ZrO₂ (800) was determined to be 16.00%, 28.45%, 40.02%, 42.50%, and 43.61%, respectively.

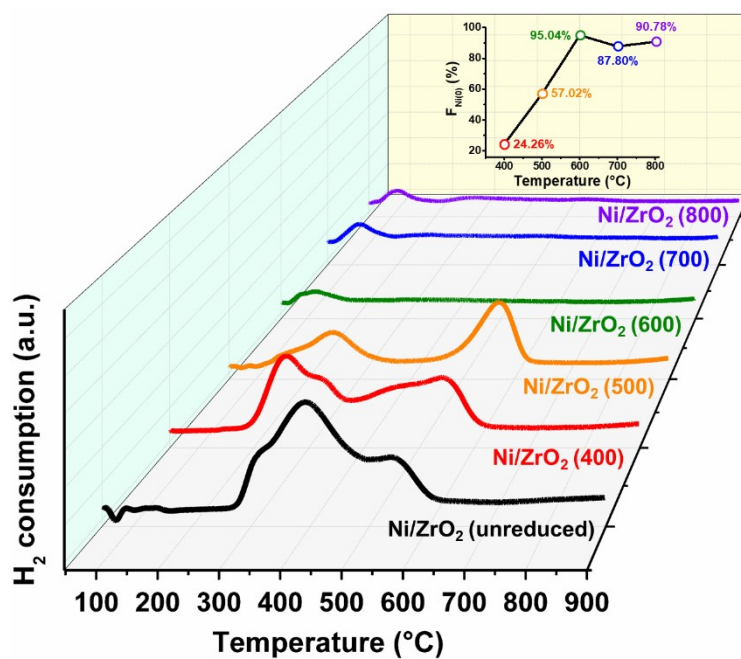


Figure S8. H₂-TPR profiles of Ni/ZrO₂ catalysts with the inserted graph illustrating the dependence of the fraction of Ni metal on the reducing temperature.

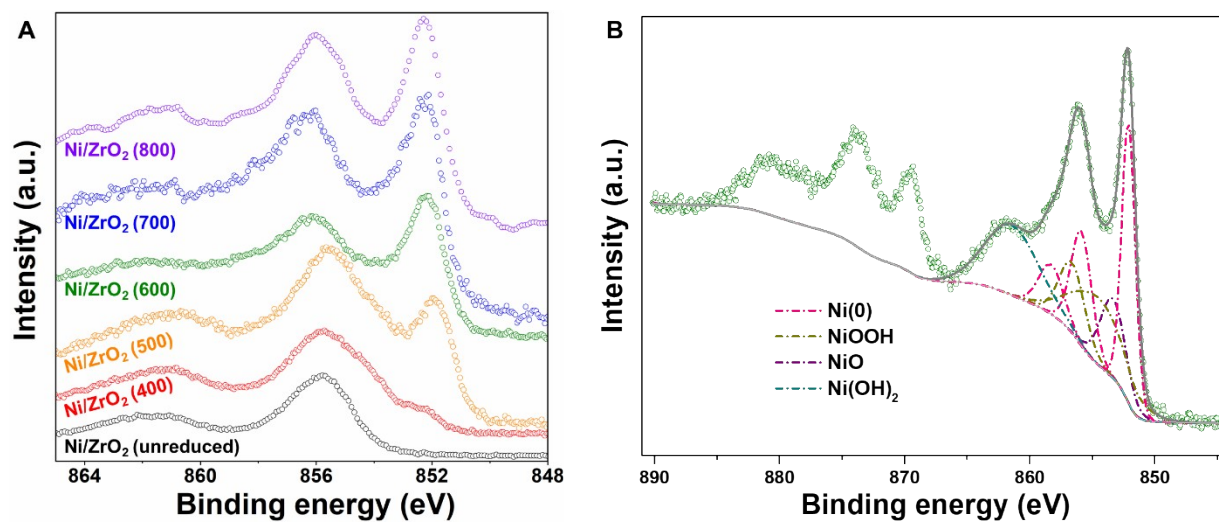


Figure S9. XPS spectra of Ni/ZrO₂ catalysts
 (A) Ni_{2p_{3/2}} spectra of various Ni/ZrO₂ catalysts.
 (B) Ni_{2p} spectrum of Ni/ZrO₂ (600) with deconvoluted peaks of Ni_{2p_{3/2}} band.

3.6. Initial rates or TOFs of photocatalytic hydrogenolysis of BPE or PPE under different light conditions and reaction temperatures

Both light and reaction temperature are key factors influencing photocatalytic reactions. For the currently studied light-driven catalysis on Ni Nanoparticles, the study on the effects of light intensity, wavelength, and reaction temperature will provide crucial insights into the light-induced mechanism.^[82,83] These experimental procedures have been widely accepted to be simple but effective in distinguishing photothermal from hot-carrier processes.^[50,84] Here we conducted several sets of reactions to obtain the initial rates of photocatalytic hydrogenolysis of BPE or PPE under different light conditions and reaction temperatures (Figure S10-S12). The conversions of all these reactions were below 30% and only the cleavage of C_{aryl}-O bonds in BPE (or PPE) occurred to produce equimolar toluene (or ethylbenzene) and phenol. The dependence of the initial TOF of photocatalytic and thermocatalytic hydrogenolysis of PPE on the reaction temperature is also provided in Figure S13, based on which the apparent activation energy can be obtained by fitting the temperature-dependent TOF with the Arrhenius equation. For the hydrogenolysis of PPE, applying visible light with 0.5 W·cm⁻² intensity induces a 27.8% decrease of the apparent activation energy on the Ni/ZrO₂ catalyst.

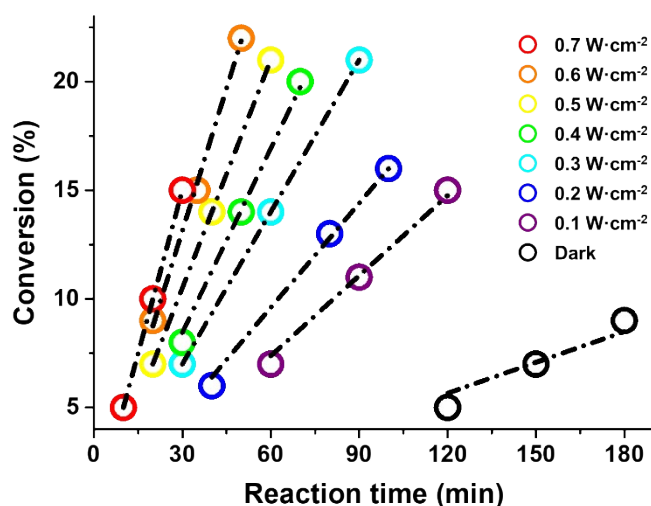


Figure S10. Calculation of the initial reaction rates of photocatalytic hydrogenolysis of BPE under various intensities of visible light. Reaction conditions: BPE 0.05 mmol, 2-butanol 2 mL, Ni/ZrO₂ 20 mg, hydrazine hydrate 0.05 mmol (1.0 equiv.), 40 °C.

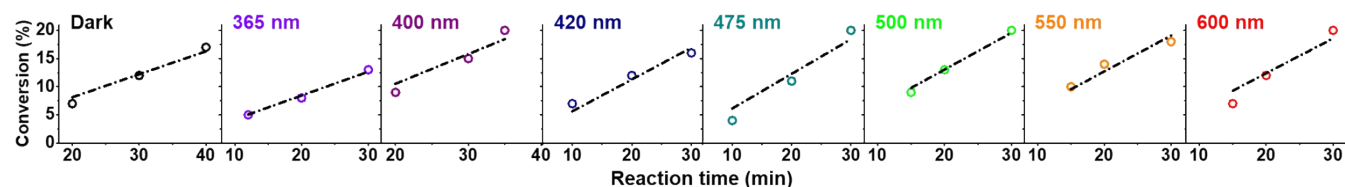


Figure S11. Calculation of the initial reaction rates of photocatalytic hydrogenolysis of BPE under different wavelengths. Reaction conditions: BPE 0.05 mmol, 2-butanol 2 mL, Ni/ZrO₂ 20 mg, hydrazine hydrate 0.05 mmol (1.0 equiv.), 60 °C.

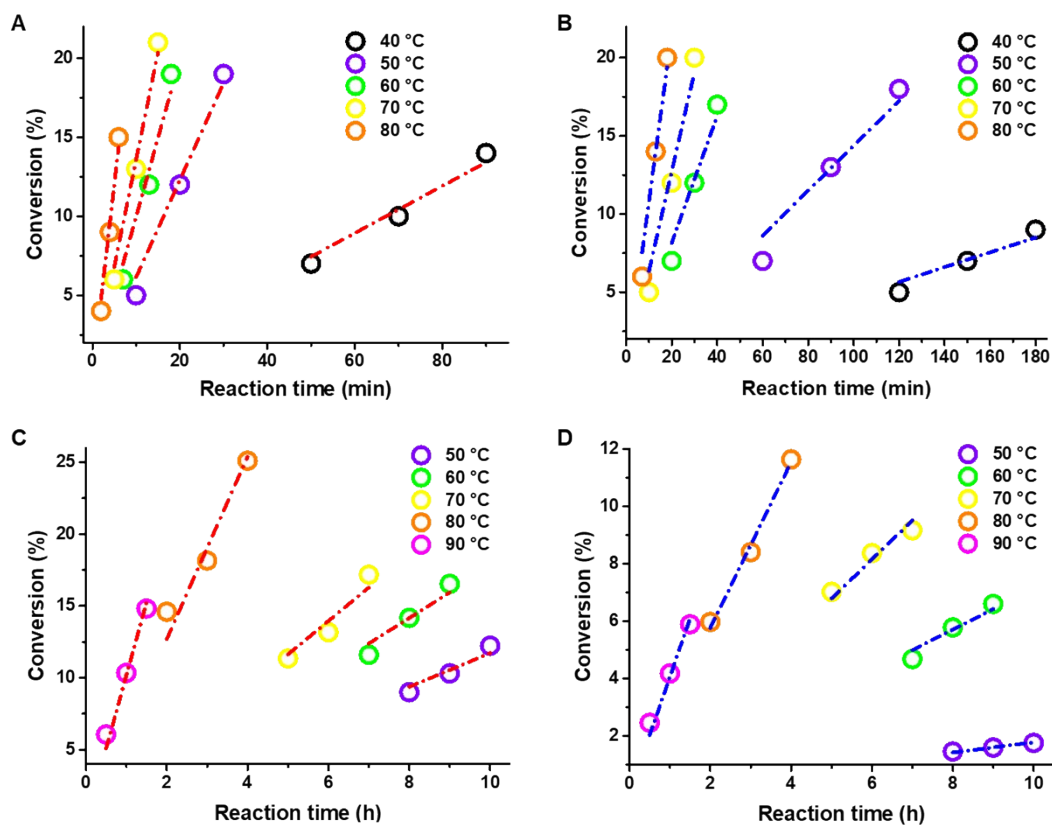


Figure S12. Calculation of the initial reaction rates of photocatalytic hydrogenolysis of BPE or PPE at different reaction temperatures (A) BPE under $0.2 \text{ W}\cdot\text{cm}^{-2}$ intensity of LED light, (B) BPE under dark, (C) PPE under $0.5 \text{ W}\cdot\text{cm}^{-2}$ intensity of LED light, (D) PPE under dark. Reaction conditions: BPE or PPE 0.05 mmol , 2-butanol 2 mL , Ni/ZrO_2 20 mg , hydrazine hydrate 0.05 mmol (1.0 equiv.).

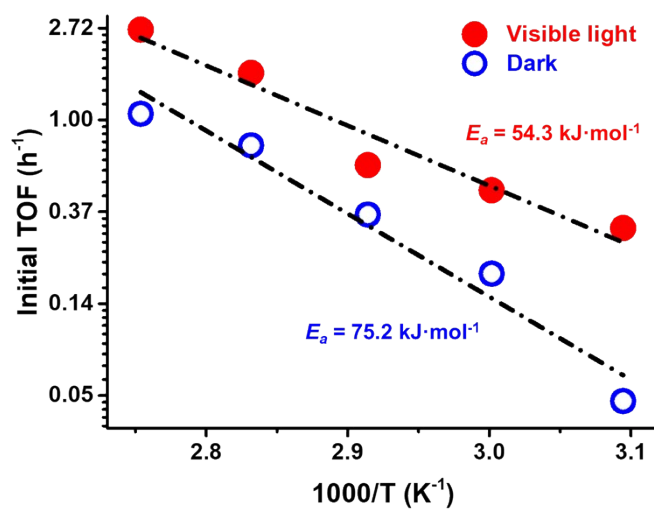
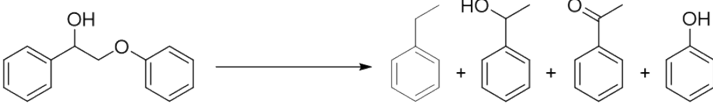


Figure S13. Initial TOF of photocatalytic and thermocatalytic hydrogenolysis of PPE as a function of reaction temperature with the obtained apparent activation energy values by fitting with the Arrhenius equation.

3.7. Radical scavenger study

This redox-neutral cleavage of PP-ol can start with the generation of a C_α radical intermediate through the C_α-H bond scission,^[17,18] or with the generation of PP-one intermediate through a reversible dehydrogenation of PP-ol at C_α position.^[74] Wu et al. found that the C_α-H bond scission produced a radical intermediate with a much weaker ether C-O bond (BDE decreased by 85.8%) so that the ether bond cleavage of this intermediate could proceed under mild conditions.^[17] So we further conducted control experiments using two radical scavengers, DMPO and PBN,^[17,18] to investigate if the above mentioned radical mechanism is responsible for the photocatalytic cleavage of PP-ol. The results presented in Scheme S5 showed that neither DMPO nor PBN affected the photocatalytic cleavage of PP-ol, illustrating that this radical process can be ruled out.



The reaction scheme shows the photocatalytic cleavage of PP-ol (1-phenylethyl phenyl ether) into four products: ethylbenzene, 1-phenylethanol, acetophenone, and phenol. The conversion and yield percentages for each condition are summarized in the table below.

	Conversion (%)	Yield (%)	Yield (%)	Yield (%)	Yield (%)
Without scavenger	96	3	38	14	41
Radical scavenger (DMPO)	96	1	38	16	41
Radical scavenger (PBN)	93	1	36	16	40

Scheme S5. Effects of radical scavengers on the photocatalytic cleavage of PP-ol on Ni/ZrO₂ under visible light irradiation.

Reaction conditions: PP-ol 0.05 mmol, 2-butanol 2 mL, Ni/ZrO₂ 20 mg, hydrazine hydrate 0.05 mmol (1.0 equiv.), DMPO or PBN 0.05 mmol (1.0 equiv.), 0.5 W·cm⁻² intensity of LED light, r.t., 15 h.

3.8. Kinetics study for the photocatalytic cleavage of PP-one

Kinetics profiles of the photocatalytic cleavage of PP-one under both visible light (Figure 4C) and dark (Figure 4D) conditions showed abrupt changes of PP-one and PP-ol. To further explore this phenomenon, here we show the changes of PP-one and PP-ol during the reaction under visible light (Figure S14A) and dark (Figure S14B), together with the change of phenol which indicates the cleavage of the β -O-4 linkage in dimer compounds. We also calculated the ratio of molar concentration of PP-ol to the sum of molar concentration of PP-ol and PP-one as given in Figure S14C. Under visible light irradiation, about 10% of PP-one was cleaved into monomers in the first hour, while the hydrogenation of PP-one to PP-ol did not occur. After that, a fast transformation of PP-one to PP-ol was observed during 1-2 hour and PP-ol accounted for 60% of the dimer compounds. Under dark condition, no PP-ol was formed during the first 6 hours, during which about 10% of PP-one was cleaved into monomers. In the following 3 hours, a fast transformation of PP-one to PP-ol was also observed and PP-ol accounted for 60% of the dimer compounds at the reaction time of 9 h. These results indicated that under both visible light and dark conditions, a fast hydrogenation of PP-one to PP-ol catalyzed by Ni/ZrO₂ took place after the initial stage of the reaction during which about 10% of PP-one was cleaved into its monomer products.

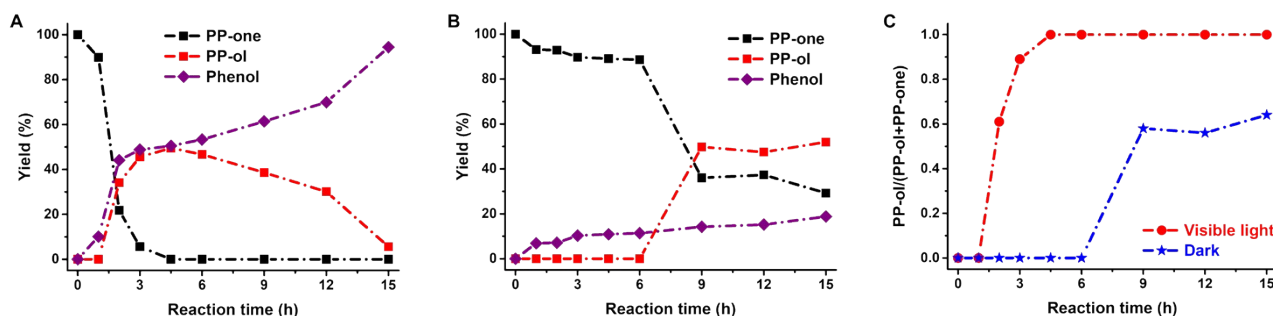


Figure S14. Kinetics profiles of the photocatalytic cleavage of PP-one on Ni/ZrO₂

(A) Yields of PP-one, PP-ol, and phenol during the reaction under visible light, (B) yields of these three substrates during the reaction under dark, (C) ratio of molar concentration of PP-ol to the sum of molar concentration of PP-ol and PP-one.

Yield of a specific substance was calculated by dividing the molar concentration of the substance by the initial molar concentration of PP-one and multiplying by 100%.

Reaction conditions: PP-one 0.05 mmol, 2-butanol 2 mL, Ni/ZrO₂ 20 mg, hydrazine hydrate 0.05 mmol (1.0 equiv.), r.t., 0.5 W·cm⁻² intensity of LED light.

3.9. Recycling of the Ni/ZrO₂ catalyst

The recyclability of the Ni/ZrO₂ catalyst was investigated for five successive cycles. Figure S15 presents the conversion of BPE and the selectivity of the two aromatic monomer products. After the first cycle, the conversion of BPE decreased by ~30% and maintained at about 70% for the following cycles. The selectivity did not show obvious changes during the recycling experiments. Several characterization techniques were employed to analyze the recycled catalysts. ICP-OES analysis showed that the exact Ni content of Ni/ZrO₂ after five cycles was 8.46 ± 0.04 wt.%, which was very close to the original Ni content (8.66 ± 0.14 wt.%). TEM image of the Ni/ZrO₂ catalyst after five cycles is provided in Figure S16A. The average size of Ni nanoparticles was determined to be 6.6 ± 1.2 nm, which meant Ni nanoparticles did not grow up obviously after recycled. Figure S16B shows the XPS spectra of the recycled Ni/ZrO₂ catalysts together with the fraction of Ni metal at the surface calculated using the fitting procedures mentioned above. In Figure S16B, Ni/ZrO₂-X (X = I, II, III, IV, V) means the catalyst tested for cycle X, and Ni/ZrO₂-X' (X = I, II, III, IV, V) means the used Ni/ZrO₂-X catalyst before the thermal reducing treatment. After the first cycle, the fraction of Ni metal at the surface decreased obviously from 40.02% to 16.74% and then increased to 29.25% after the thermal reducing treatment. For the following cycles, the fraction of Ni metal at the surface could be kept at about 30% by the thermal reducing treatment. XPS results clearly demonstrated that the change of the surface content of Ni metal was responsible for the observed change of the photocatalytic performance as shown in Figure S15.

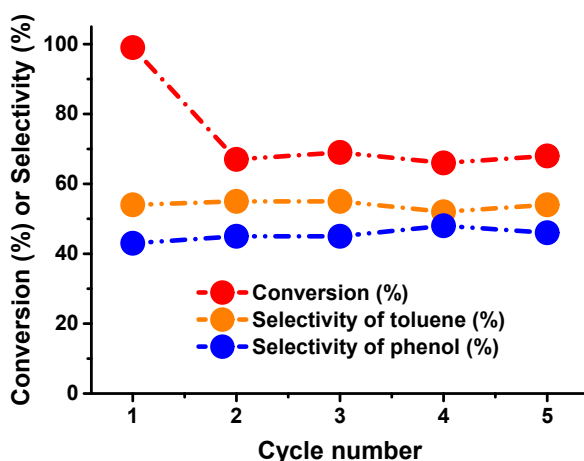


Figure S15. Photocatalytic performance of Ni/ZrO₂ for the hydrogenolysis of BPE during five successive cycles. Reaction conditions: BPE 0.05 mmol, 2-butanol 2 mL, Ni/ZrO₂ 20 mg, hydrazine hydrate 0.05 mmol (1.0 equiv.), 0.5 W·cm⁻² intensity of LED light, r.t., 13 h.

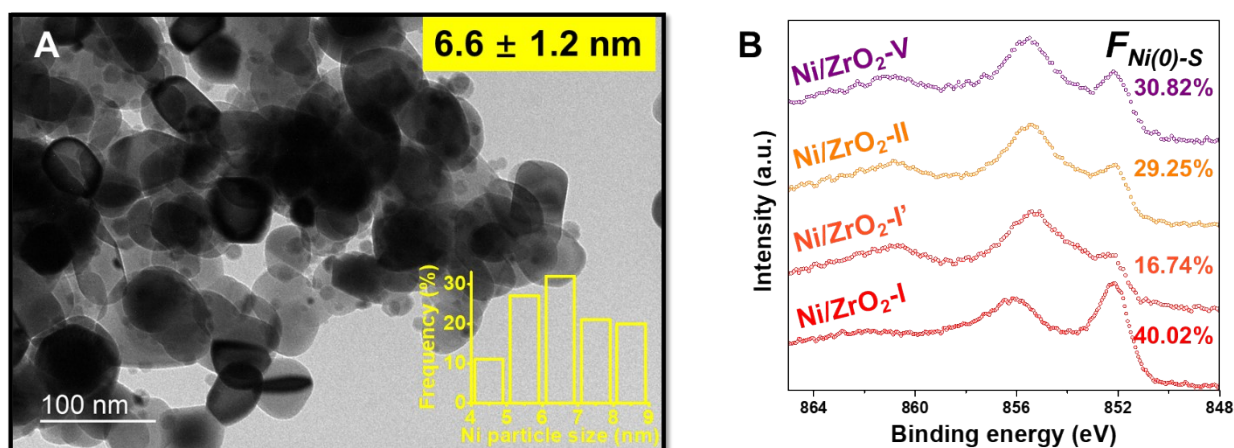


Figure S16. Characterization of the recycled Ni/ZrO₂ catalysts (A) TEM image of the Ni/ZrO₂ catalyst after five cycles with the inserted histogram of size distribution of Ni nanoparticles. (B) XPS spectra with the fraction of Ni metal at the surface.

4. References

1. Li, C., Zhao, X., Wang, A., Huber, G.W., and Zhang, T. (2015). Catalytic Transformation of Lignin for the Production of Chemicals and Fuels. *Chem. Rev.* **115**, 11559-11624. 10.1021/acs.chemrev.5b00155.
2. Wang, H., Pu, Y., Ragauskas, A., and Yang, B. (2019). From Lignin to Valuable Products-Strategies, Challenges, and Prospects. *Bioresour. Technol.* **271**, 449-461. 10.1016/j.biortech.2018.09.072.
3. Amidon, T.E., and Liu, S. (2009). Water-Based Woody Biorefinery. *Biotechnol. Adv.* **27**, 542-550. 10.1016/j.biotechadv.2009.04.012.
4. Gillet, S., Aguedo, M., Petitjean, L., Morais, A.R.C., da Costa Lopes, A.M., Łukasik, R.M., and Anastas, P.T. (2017). Lignin Transformations for High Value Applications: towards Targeted Modifications Using Green Chemistry. *Green Chem.* **19**, 4200-4233. 10.1039/C7GC01479A.
5. Xu, C., Arancon, R.A.D., Labidi, J., and Luque, R. (2014). Lignin Depolymerisation Strategies: Towards Valuable Chemicals and Fuels. *Chem. Soc. Rev.* **43**, 7485-7500. 10.1039/c4cs00235k.
6. Wang, M., and Wang, F. (2019). Catalytic Scissoring of Lignin into Aryl Monomers. *Adv. Mater.* **31**, 1901866. 10.1002/adma.201901866.
7. Zhang, J., Teo, J., Chen, X., Asakura, H., Tanaka, T., Teramura, K., and Yan, N. (2014). A Series of NiM (M = Ru, Rh, and Pd) Bimetallic Catalysts for Effective Lignin Hydrogenolysis in Water. *ACS Catal.* **4**, 1574-1583. 10.1021/cs401199f.
8. Sun, Z., Fridrich, B., de Santi, A., Elangovan, S., and Barta, K. (2018). Bright Side of Lignin Depolymerization: Toward New Platform Chemicals. *Chem. Rev.* **118**, 614-678. 10.1021/acs.chemrev.7b00588.
9. Rinaldi, R., Jastrzebski, R., Clough, M.T., Ralph, J., Kennema, M., Bruijninx, P.C., and Weckhuysen, B.M. (2016). Paving the Way for Lignin Valorisation: Recent Advances in Bioengineering, Biorefining and Catalysis. *Angew. Chem. Int. Ed.* **55**, 8164-8215. 10.1002/anie.201510351.
10. Holladay, J.E., White, J.F., Bozell, J.J., and Johnson, D. (2007). Top Value Added Chemicals from Biomass, Volume II-Results of Screening for Potential Candidates from Biorefinery Lignin. Pacific Northwest Laboratory (PNNL), Richland WA (USA).
11. Gazi, S. (2019). Valorization of Wood Biomass-Lignin via Selective Bond Scission: A Minireview. *Appl. Catal., B* **257**, 117936. 10.1016/j.apcatb.2019.117936.
12. He, J., Zhao, C., and Lercher, J.A. (2012). Ni-Catalyzed Cleavage of Aryl Ethers in the Aqueous Phase. *J. Am. Chem. Soc.* **134**, 20768-20775. 10.1021/ja309915e.
13. Stavila, V., Parthasarathi, R., Davis, R.W., El Gabaly, F., Sale, K.L., Simmons, B.A., Singh, S., and Allendorf, M.D. (2016). MOF-Based Catalysts for Selective Hydrogenolysis of Carbon-Oxygen Ether Bonds. *ACS Catal.* **6**, 55-59. 10.1021/acscatal.5b02061.
14. Bulut, S., Siankevich, S., van Muyden, A.P., Alexander, D.T., Savoglidis, G., Zhang, J., Hatzimanikatis, V., Yan, N., and Dyson, P.J. (2018). Efficient Cleavage of Aryl Ether C-O Linkages by Rh-Ni and Ru-Ni Nanoscale Catalysts Operating in Water. *Chem. Sci.* **9**, 5530-5535. 10.1039/C8SC00742J.
15. Mauriello, F., Paone, E., Pietropaolo, R., Balu, A.M., and Luque, R. (2018). Catalytic Transfer Hydrogenolysis of Lignin-Derived Aromatic Ethers Promoted by Bimetallic Pd/Ni Systems. *ACS Sustain. Chem. Eng.* **6**, 9269-9276. 10.1021/acssuschemeng.8b01593.
16. Rahimi, A., Ulbrich, A., Coon, J.J., and Stahl, S.S. (2014). Formic-Acid-Induced Depolymerization of Oxidized Lignin to Aromatics. *Nature* **515**, 249-252. 10.1038/nature13867.
17. Wu, X., Fan, X., Xie, S., Lin, J., Cheng, J., Zhang, Q., Chen, L., and Wang, Y. (2018). Solar Energy-Driven Lignin-First Approach to Full Utilization of Lignocellulosic Biomass under Mild Conditions. *Nat. Catal.* **1**, 772-780. 10.1038/s41929-018-0148-8.
18. Yoo, H., Lee, M.W., Lee, S., Lee, J., Cho, S., Lee, H., Cha, H.G., and Kim, H.S. (2020). Enhancing Photocatalytic β -O-4 Bond Cleavage in Lignin Model Compounds by Silver-Exchanged Cadmium Sulfide. *ACS Catal.* **10**, 8465-8475. 10.1021/acscatal.0c01915.
19. Zaheer, M., and Kempe, R. (2015). Catalytic Hydrogenolysis of Aryl Ethers: A Key Step in Lignin Valorization to Valuable Chemicals. *ACS Catal.* **5**, 1675-1684. 10.1021/cs501498f.
20. Ji, J., Guo, H., Li, C., Qi, Z., Zhang, B., Dai, T., Jiang, M., Ren, C., Wang, A., and Zhang, T. (2018). Tungsten-Based Bimetallic Catalysts for Selective Cleavage of Lignin C-O Bonds. *ChemCatChem* **10**, 415-421. 10.1002/cctc.201701240.
21. Zhang, J., Ibrahim, M., Collière, V., Asakura, H., Tanaka, T., Teramura, K., Philippot, K., and Yan, N. (2016). Rh Nanoparticles with NiO_x Surface Decoration for Selective Hydrogenolysis of C-O Bond over Arene Hydrogenation. *J. Mol. Catal. A: Chem.* **422**, 188-197. 10.1016/j.molcata.2016.01.014.
22. Zhang, J., Cai, Y., Lu, G., and Cai, C. (2016). Facile and Selective Hydrogenolysis of β -O-4 Linkages in Lignin Catalyzed by Pd-Ni Bimetallic Nanoparticles Supported on ZrO₂. *Green Chem.* **18**, 6229-6235. 10.1039/C6GC02265K.
23. Wu, H., Song, J., Xie, C., Wu, C., Chen, C., and Han, B. (2018). Efficient and Mild Transfer Hydrogenolytic Cleavage of Aromatic Ether Bonds in Lignin-Derived Compounds Over Ru/C. *ACS Sustain. Chem. Eng.* **6**, 2872-2877. 10.1021/acssuschemeng.7b02993.
24. Malara, A., Paone, E., Bonaccorsi, L., Mauriello, F., Macario, A., and Frontera, P. (2020). Pd/Fe₃O₄ Nanofibers for the Catalytic Conversion of Lignin-Derived Benzyl Phenyl Ether under Transfer Hydrogenolysis Conditions. *Catalysts* **10**, 20. 10.3390/catal10010020.
25. Zhu, C., Cao, J.-P., Zhao, X.-Y., Xie, T., Zhao, M., and Wei, X.-Y. (2019). Bimetallic Effects in the Catalytic Hydrogenolysis of Lignin and its Model Compounds on Nickel-Ruthenium Catalysts. *Fuel Process. Technol.* **194**, 106126. 10.1016/j.fuproc.2019.106126.
26. Sergeev, A.G., and Hartwig, J.F. (2011). Selective, Nickel-Catalyzed Hydrogenolysis of Aryl Ethers. *Science* **332**, 439-443. 10.1126/science.1200437.
27. Gao, F., Webb, J.D., and Hartwig, J.F. (2016). Chemo- and Regioselective Hydrogenolysis of Diaryl Ether C-O Bonds by a Robust Heterogeneous Ni/C Catalyst: Applications to the Cleavage of Complex Lignin-Related Fragments. *Angew. Chem. Int. Ed.* **55**, 1474-1478. 10.1002/anie.201622030.
28. Ren, Y., Yan, M., Wang, J., Zhang, Z.C., and Yao, K. (2013). Selective Reductive Cleavage of Inert Aryl C-O Bonds by an Iron Catalyst. *Angew. Chem. Int. Ed.* **52**, 12674-12678. 10.1002/anie.201305342.
29. Molinari, V., Giordano, C., Antonietti, M., Esposito, D. (2014). Titanium Nitride-Nickel Nanocomposite as Heterogeneous Catalyst for the Hydrogenolysis of Aryl Ethers. *J. Am. Chem. Soc.* **136**, 1758-1761. 10.1021/ja4119412.
30. Zaheer, M., Hermannsdörfer, J., Kretschmer, W.P., Motz, G., and Kempe, R. (2014). Robust Heterogeneous Nickel Catalysts with Tailored Porosity for the Selective Hydrogenolysis of Aryl Ethers. *ChemCatChem* **6**, 91-95. 10.1002/cctc.201300763.
31. Cui, X., Yuan, H., Junge, K., Topf, C., Beller, M., and Shi, F. (2017). A Stable and Practical Nickel Catalyst for the Hydrogenolysis of C-O bonds. *Green Chem.* **19**, 305-310. 10.1039/C6GC01955B.
32. Li, J., Sun, H., Liu, J., Zhang, J., Li, Z., and Fu, Y. (2018). Selective Reductive Cleavage of C-O Bond in Lignin Model Compounds over Nitrogen-Doped Carbon-Supported Iron Catalysts. *Mol. Catal.* **452**, 36-45. 10.1016/j.mcat.2018.03.014.
33. Song, Y., Li, Z., Ji, P., Kaufmann, M., Feng, X., Chen, J.S., Wang, C., and Lin, W. (2019). Metal-Organic Framework Nodes Support Single Site Nickel(II) Hydride Catalysts for the Hydrogenolysis of Aryl Ethers. *ACS Catal.* **9**, 1578-1583. 10.1021/acscatal.8b04611.
34. Jiang, L., Guo, H., Li, C., Zhou, P., and Zhang, Z. (2019). Selective Cleavage of Lignin and Lignin Model Compounds without External Hydrogen, Catalyzed by Heterogeneous Nickel Catalysts. *Chem. Sci.* **10**, 4458-4468. 10.1039/C9SC00691E.
35. Wu, X., Luo, N., Xie, S., Zhang, H., Zhang, Q., Wang, F., and Wang, Y. (2020). Photocatalytic Transformations of Lignocellulosic Biomass into Chemicals. *Chem. Soc. Rev.* **49**, 6198-6223. 10.1039/D0CS00314J.

36. Luo, N., Wang, M., Li, H., Zhang, J., Liu, H., and Wang, F. (2016). Photocatalytic Oxidation-Hydrogenolysis of Lignin β -O-4 Models via Dual Light Wavelength Switching Strategy. *ACS Catal.* **6**, 7716-7721. 10.1021/acscatal.6b02212.
37. Luo, N., Wang, M., Li, H., Zhang, J., Hou, T., Chen, H., Zhang, X., Lu, J., and Wang, F. (2017). Visible-Light-Driven Self-Hydrogen Transfer Hydrogenolysis of Lignin Models and Extracts into Phenolic Products. *ACS Catal.* **7**, 4571-4580. 10.1021/acscatal.7b01043.
38. Han, G., Yan, T., Zhang, W., Zhang, Y.C., Lee, D.Y., Cao, Z., and Sun, Y. (2019). Highly Selective Photocatalytic Valorization of Lignin Model Compounds Using Ultrathin Metal/CdS. *ACS Catal.* **9**, 11341-11349. 10.1021/acscatal.9b02842.
39. Aslam, U., Rao, V. G., Chavez, S., and Linic, S. (2018). Catalytic Conversion of Solar to Chemical Energy on Plasmonic Metal Nanostructures. *Nat. Catal.* **1**, 656-665. 10.1038/s41929-018-0138-x.
40. Kim, C., Hyeon, S., Lee, J., Kim, W. D., Lee, D. C., Kim, J., and Lee, H. (2018). Energy-Efficient CO₂ Hydrogenation with Fast Response Using Photoexcitation of CO₂ Adsorbed on Metal Catalysts. *Nat. Commun.* **9**, 3027. 10.1038/s41467-018-05542-5.
41. Ertl, G. (2008). Reactions at Surfaces: from Atoms to Complexity (Nobel Lecture). *Angew. Chem. Int. Ed.* **47**, 3524-3535. 10.1002/anie.200800480.
42. Kim, C., and Lee, H. (2018). Light-Assisted Surface Reactions on Metal Nanoparticles. *Catal. Sci. Technol.* **8**, 3718-3727. 10.1039/c8cy00674a.
43. Gellé, A., Jin, T., De La Garza, L., Price, G. D., Besteiro, L. V., and Moores, A. (2020). Applications of Plasmon-Enhanced Nanocatalysis to Organic Transformations. *Chem. Rev.* **120**, 986-1041. 10.1021/acs.chemrev.9b00187.
44. Zhang, X., Li, X., Zhang, D., Su, N. Q., Yang, W., Everitt, H. O., and Liu, J. (2017). Product Selectivity in Plasmonic Photocatalysis for Carbon Dioxide Hydrogenation. *Nat. Commun.* **8**, 14542. 10.1038/ncomms14542.
45. Ke, X., Sarina, S., Zhao, J., Zhang, X., Chang, J., and Zhu, H. (2012). Tuning the Reduction Power of Supported Gold Nanoparticle Photocatalysts for Selective Reductions by Manipulating the Wavelength of Visible Light Irradiation. *Chem. Commun.* **48**, 3509-3511. 10.1039/c2cc17977f.
46. Tana, T., Guo, X. W., Xiao, Q., Huang, Y., Sarina, S., Christopher, P., Jia, J., Wu, H., and Zhu, H. (2016). Non-Plasmonic Metal Nanoparticles as Visible Light Photocatalysts for the Selective Oxidation of Aliphatic Alcohols with Molecular Oxygen at Near Ambient Conditions. *Chem. Commun.* **52**, 11567-11570. 10.1039/c6cc05186c.
47. Sarina, S., Jaatinen, E., Xiao, Q., Huang, Y.M., Christopher, P., Zhao, J.C., and Zhu, H.-Y. (2017). Photon Energy Threshold in Direct Photocatalysis with Metal Nanoparticles: Key Evidence from the Action Spectrum of the Reaction. *J. Phys. Chem. Lett.* **8**, 2526-2534. 10.1021/acs.jpcclett.7b00941.
48. Meng, X., Wang, T., Liu, L., Ouyang, S., Li, P., Hu, H., Kako, T., Iwai, H., Tanaka, A., and Ye, J. (2014). Photothermal Conversion of CO₂ into CH₄ with H₂ over Group VIII Nanocatalysts: An Alternative Approach for Solar Fuel Production. *Angew. Chem. Int. Ed.* **53**, 11478-11482. 10.1002/anie.201404953.
49. Swearer, D. F., Robatjazi, H., Martinez, J. M. P., Zhang, M., Zhou, L., Carter, E. A., Nordlander, P., and Halas, N. J. (2019). Plasmonic Photocatalysis of Nitrous Oxide into N₂ and O₂ Using Aluminum-Iridium Antenna-Reactor Nanoparticles. *ACS Nano* **13**, 8076-8086. 10.1021/acsnano.9b02924.
50. Baffou, G., Bordacchini, I., Baldi, A., and Quidant, R. (2020). Simple Experimental Procedures to Distinguish Photothermal from Hot-Carrier Processes in Plasmonics. *Light: Sci. Appl.* **9**, 108. 10.1038/s41377-020-00345-0.
51. Christopher, P., Xin, H., Marimuthu, A., and Linic, S. (2012). Singular Characteristics and Unique Chemical Bond Activation Mechanisms of Photocatalytic Reactions on Plasmonic Nanostructures. *Nat. Mater.* **11**, 1044-1050. 10.1038/nmat3454.
52. Lindstrom, C. D. and Zhu, X.-Y. (2006). Photoinduced Electron Transfer at Molecule-Metal Interfaces. *Chem. Rev.* **106**, 4281-4300. 10.1021/cr0501689.
53. Mao, Z., Espinoza, R., Garcia, A., Enwright, A., Vang, H., and Nguyen, S. C. (2020). Tuning Redox Potential of Gold Nanoparticle Photocatalysts by Light. *ACS Nano* **14**, 7038-7045. 10.1021/acsnano.0c01704.
54. Smith, J. G., Fauchaux, J. A., & Jain, P. K. (2015). Plasmon Resonances for Solar Energy Harvesting: A Mechanistic Outlook. *Nano Today* **10**, 67-80. 10.1016/j.nantod.2014.12.004.
55. Thompson, T. L. and Yates, J. T. Jr (2010) Monitoring Hole Trapping in Photoexcited TiO₂(110) Using a Surface Photoreaction. *J. Phys. Chem B* **109**, 18230-18236. 10.1021/jp0530451.
56. Westrich, T. A., Dahlberg, K. A., Kaviany, M., and Schwank, J. W. High-Temperature Photocatalytic Ethylene Oxidation over TiO₂. *J. Phys. Chem. C* **2011**, **115**, 16537-16543. 10.1021/jp204405h.
57. Sarina, S., Zhu, H.-Y., Xiao, Q., Jaatinen, E., Jia, J., Huang, Y., Zheng, Z., and Wu, H. (2014). Viable Photocatalysts under Solar-Spectrum Irradiation: Nonplasmonic Metal Nanoparticles. *Angew. Chem. Int. Ed.* **53**, 2935-2940. 10.1002/anie.201308145.
58. Kale, M. J., Avanesian, T., Xin, H., Yan, J., and Christopher, P. (2014). Controlling Catalytic Selectivity on Metal Nanoparticles by Direct Photoexcitation of Adsorbate-Metal Bonds. *Nano Lett.* **14**, 5405-5412. 10.1021/nl502571b.
59. Guo, X.-N., Jiao, Z.-F., Jin, G.-Q., and Guo, X.-Y. (2015). Photocatalytic Fischer-Tropsch Synthesis on Graphene-Supported Worm-Like Ruthenium Nanostructures. *ACS Catal.* **5**, 3836-3840. 10.1021/acscatal.5b00697.
60. Linic, S., Aslam, U., Boerigter, C., and Morabito, M. (2015). Photochemical Transformations on Plasmonic Metal Nanoparticles. *Nat. Mater.* **14**, 567-576. 10.1038/nmat4281.
61. Linic, S., Chavez, S., and Elias, R. (2021). Flow and Extraction of Energy and Charge Carriers in Hybrid Plasmonic Nanostructures. *Nat. Mater.* **20**, 916-924. 10.1038/s41563-020-00858-4.
62. Sytwu, K., Vadai, M., and Dionne, J. A. (2019). Bimetallic Nanostructures: Combining Plasmonic and Catalytic Metals for Photocatalysis. *Adv. Phys.: X* **4**, 1619480. 10.1080/23746149.2019.1619480.
63. Peiris, E., Sarina, S., Waclawik, E. R., Ayoko, G. A., Han, P., Jia, J., and Zhu, H.-Y. (2019). Plasmonic Switching of the Reaction Pathway: Visible-Light Irradiation Varies the Reactant Concentration at the Solid-Solution Interface of a Gold-Cobalt Catalyst. *Angew. Chem. Int. Ed.* **58**, 12032-12036. 10.1002/anie.201904452.
64. Aslam, U., Chavez, S., and Linic, S. (2017). Controlling Energy Flow in Multimetallic Nanostructures for Plasmonic Catalysis. *Nat. Nanotechnol.* **12**, 1000-1005. 10.1038/nnano.2017.131.
65. Xin, Y., Yu, K., Zhang, L., Yang, Y., Yuan, H., Li, H., Wang, L., and Zeng, J. (2021). Copper-Based Plasmonic Catalysis: Recent Advances and Future Perspectives. *Adv. Mater.* 10.1002/adma.202008145.
66. Cortés, E., Besteiro, L. V., Alabastri, A., Baldi, A., Tagliabue, G., Demetriadou, A., and Narang, P. (2020). Challenges in Plasmonic Catalysis. *ACS Nano* **14**, 16202-16219. 10.1021/acsnano.0c08773.
67. Shimizu, K.I., Kon, K., Onodera, W., Yamazaki, H., and Kondo, J.N. (2013). Heterogeneous Ni Catalyst for Direct Synthesis of Primary Amines from Alcohols and Ammonia. *ACS Catal.* **3**, 112-117. 10.1021/cs3007473.
68. Gould, T.D., Lubers, A.M., Neltner, B.T., Carrier, J.V., Weimer, A.W., Falconer, J.L., and Medlin, J.W. (2013). Synthesis of Supported Ni Catalysts by Atomic Layer Deposition. *J. Catal.* **303**, 9-15. 10.1016/j.jcat.2013.03.013.
69. Xu, M., He, S., Chen, H., Cui, G., Zheng, L., Wang, B., and Wei, M. (2017). TiO_{2-x}-Modified Ni Nanocatalyst with Tunable Metal-Support Interaction for Water-Gas Shift Reaction. *ACS Catal.* **7**, 7600-7609. 10.1021/acscatal.7b01951.
70. Deepa, A.K., and Dhepe, P.L. (2015). Lignin Depolymerization into Aromatic Monomers over Solid Acid Catalysts. *ACS Catal.* **5**, 365-379. 10.1021/cs501371q.
71. Shu, R., Long, J., Xu, Y., Ma, L., Zhang, Q., Wang, T., Wang, C., Yuan, Z., and Wu, Q. (2016). Investigation on the Structural Effect of Lignin During the Hydrogenolysis Process. *Bioresour. Technol.* **200**, 14-22. 10.1016/j.biortech.2015.09.112.
72. Nandiwale, K. Y., Danby, A. M., Ramanathan, A., Chaudhari, R. V., and Subramaniam, B. (2017). Zirconium-Incorporated Mesoporous Silicates Show Remarkable Lignin Depolymerization Activity. *ACS Sustain. Chem. Eng.* **5**, 7155-7164. 10.1021/acssuschemeng.7b01344.

73. Shuai, L., Amiri, M.T., Questell-santiago, Y.M., Héroguel, F., Li, Y., Kim, H., Meilan, R., Chapple, C., Ralph, J., and Luterbacher, J.S. (2016). Formaldehyde Stabilization Facilitates Lignin Monomer Production During Biomass Depolymerization. *Science* 354, 329-333. 10.1126/science.aaf7810.
74. Galkin, M.V., Dahlstrand, C., and Samec, J.S.M. (2015). Mild and Robust Redox-Neutral Pd/C-Catalyzed Lignol β -O-4' Bond Cleavage Through a Low-Energy-Barrier Pathway. *ChemSusChem* 8, 2187-2192. 10.1002/cssc.201500117.
75. Wang, X., and Rinaldi, R. (2012). Solvent Effects on the Hydrogenolysis of Diphenyl Ether with Raney Nickel and their Implications for the Conversion of Lignin. *ChemSusChem* 5, 1455-1466. 10.1002/cssc.201200531.
76. Schneider, C.A., Rasband, W.S., and Eliceiri, K.W. (2012). NIH Image to ImageJ: 25 years of Image Analysis. *Nat. Methods* 9, 671-675. 10.1038/nmeth.2089.
77. Song, W., Zhao, C., and Lercher, J.A. (2013). Importance of Size and Distribution of Ni Nanoparticles for Hydrodeoxygenation of Microalgae Oil. *Chem. - Eur. J.* 19, 9833-9842. 10.1002/chem.201301005.
78. Wang, L., Guo, H., Chen, X., Chen, Q., Wei, X., Ding, Y., and Zhu, B. (2015). Optimization of the Catalytic Hydrogenation of Terebinth by a Ni-based Catalyst. *Catal. Sci. Technol.* 5, 3340-3351. 10.1039/c4cy01704h.
79. Zhang, J., An, Z., Zhu, Y., Shu, X., Song, H., Jiang, Y., Wang, W., Xiang, X., Xu, L., and He, J. (2019). Ni⁰/Ni²⁺ Synergistic Catalysis on a Nanosized Ni Surface for Simultaneous Formation of C-C and C-N Bonds. *ACS Catal.* 9, 11438-11446. 10.1021/acscatal.9b03245.
80. Biesinger, M.C., Payne, B.P., Lau, L.W.M., Gerson, A., and Smart, R.S.C. (2010). X-ray Photoelectron Spectroscopic Chemical State Quantification of Mixed Nickel Metal, Oxide and Hydroxide Systems. *Surf. Interface Anal.* 41, 324-332. 10.1002/sia.3026.
81. Charvieux, A., Giorgi, J. B., Duguet, N., and Métay, E. (2018). Solvent-Free Direct α -Alkylation of Ketones by Alcohols Catalyzed by Nickel Supported on Silica-Alumina. *Green Chem.* 20, 4210-4216. 10.1039/C8GC01958D.
82. Li, P., Xiao, G., Zhao, Y., and Su, H. (2020). Tuning the Product Selectivity of the α -Alkylation of Ketones with Primary Alcohols using Oxidized Titanium Nitride Photocatalysts and Visible Light. *ACS Catal.* 10, 3640-3649. 10.1021/acscatal.9b04921.
83. Xiao, G., Li, P., Zhao, Y., Xu, S., and Su, H. (2018). Visible-Light-Driven Chemoselective Hydrogenation of Nitroarenes to Anilines in Water through Graphitic Carbon Nitride Metal-Free Photocatalysis. *Chem. - Asian J.* 13, 1950-1955. 10.1002/asia.201800515.
84. Zhou, L., Swearer, D.F., Zhang, C., Robatjazi, H., Zhao, H., Henderson, L., Dong, L., Christopher, P., Carter, E.A., Nordlander, P., et al. (2018). Quantifying Hot Carrier and Thermal Contributions in Plasmonic Photocatalysis. *Science* 362, 69-72. 10.1126/science.aat6967.